

SuperLocalMemory V3: Information-Geometric Foundations for Zero-LLM Enterprise Agent Memory

Varun Pratap Bhardwaj
Independent Researcher, Solution Architect
India
varun.pratap.bhardwaj@gmail.com
ORCID: 0009-0002-8726-4289

Abstract

Persistent memory is a central capability for AI agents operating across extended interactions, yet the mathematical foundations of memory retrieval, lifecycle management, and consistency remain almost entirely unexplored. Current systems predominantly employ cosine similarity for retrieval, heuristic exponential decay for salience, and provide no formal mechanism for detecting contradictions—an engineering monoculture that leaves fundamental questions of optimality, convergence, and correctness unanswered.

We establish *information-geometric foundations* for agent memory systems through three principal contributions. First, we introduce a retrieval metric derived from the Fisher information structure of diagonal Gaussian families, proving that the underlying distance satisfies Riemannian metric axioms, is invariant under sufficient statistics, and computable in $\Theta(d)$ time ([Theorem 6.1](#)). This replaces cosine similarity with a metric that weights each embedding dimension by its statistical precision. Second, we formulate memory lifecycle as Riemannian Langevin dynamics on the statistical manifold and prove existence and uniqueness of the stationary distribution via the Fokker–Planck equation ([Theorem 6.3](#)), replacing hand-tuned decay with a principled equilibrium to which the system provably converges. Third, we model the memory store as a cellular sheaf and show that non-trivial first cohomology classes correspond precisely to irreconcilable contradictions across memory contexts—an algebraic consistency guarantee that no prior system provides.

Empirically, on the LoCoMo conversational memory benchmark [\[30\]](#), the three mathematical layers yield +12.7 percentage points average improvement over the engineering baseline across six conversations ($n = 832$ questions), reaching +19.9 pp on the most challenging dialogues. The four-channel retrieval architecture achieves 75% retrieval accuracy on LoCoMo without cloud dependency during retrieval. Initial cloud-augmented results on a single conversation ($n = 81$) reach 87.7%. A zero-LLM operating configuration satisfies data sovereignty requirements under Regulation (EU) 2024/1689 by architectural design. To our knowledge, this is the first work to establish information-geometric, sheaf-theoretic, and stochastic-dynamical foundations for AI agent memory systems. We release all code under the MIT license for reproducibility at <https://github.com/qualixar/superlocalmemory>.

1 Introduction

The scaling of large language models has yielded agents capable of complex reasoning, tool use, and multi-step planning. Yet a fundamental asymmetry persists: while model capabilities have advanced by orders of magnitude, the memory systems that these agents rely on for persistent knowledge remain mathematically rudimentary. As agents are deployed in multi-session conversations, long-horizon task execution, and collaborative workflows, the absence of principled memory foundations constitutes a bottleneck not merely of engineering convenience, but of theoretical soundness.

This paper addresses a question that, to the best of our knowledge, has not been posed in the literature: *what mathematical structures are appropriate for the retrieval, lifecycle management, and consistency verification of persistent agent memory?* We answer this question by drawing on information geometry [4], algebraic topology [44], and stochastic dynamics on Riemannian manifolds [40]—three branches of mathematics with deep structural relevance to the problems at hand, but which have not been connected to agent memory systems.

The mathematical poverty of current memory systems. A striking uniformity characterizes the memory systems introduced in recent years. Every system we surveyed—including those with significant research investment [33, 38, 39] and recent academic contributions [1, 2, 17, 29]—retrieves memories via cosine similarity over dense embeddings [26, 42], manages salience through fixed exponential decay or time-to-live windows, and provides no formal mechanism for detecting contradictions across contexts. A recent survey [28] documents this pattern across more than thirty systems without identifying it as a research gap.

This uniformity is not merely an aesthetic concern. It reflects three concrete mathematical deficiencies that limit the reliability of agent memory at scale.

Three open problems. We identify three foundational gaps that motivate the present work.

1. **Uncertainty-blind retrieval.** Cosine similarity treats all embedding dimensions as equally reliable, computing $\text{sim}(\mathbf{u}, \mathbf{v}) = \mathbf{u}^\top \mathbf{v} / (\|\mathbf{u}\| \|\mathbf{v}\|)$ without any notion of per-dimension confidence. In practice, learned representations exhibit non-uniform variance: some dimensions capture well-established semantic distinctions while others encode noise or distributional artifacts. The Fisher information metric [4, 51] provides a principled alternative—it weights each dimension by the local curvature of the likelihood surface, which is precisely the statistical precision of that dimension. Čencov’s uniqueness theorem [51] establishes that the Fisher metric is, in a precise categorical sense, the *only* Riemannian metric on statistical manifolds that is invariant under sufficient statistics. Despite this theoretical grounding, the Fisher metric has not been applied to memory retrieval.
2. **Unprincipled lifecycle dynamics.** Current systems govern memory retention through heuristics: fixed time-to-live windows, exponential decay with manually chosen half-lives, or access-count thresholds [33, 38]. These mechanisms cannot adapt to the evolving statistical structure of the memory store—they are oblivious to the *geometry* of the space in which memories reside. Riemannian Langevin dynamics [40] offer a framework in which the curvature of the memory manifold itself drives retention and forgetting through a stochastic differential equation whose drift incorporates the Fisher information. The stationary distribution of such dynamics, when it exists, defines a principled equilibrium that the system converges to without hand-tuned parameters. This connection has not been explored for agent memory.
3. **Silent inconsistency.** When an agent accumulates memories across sessions, interaction partners, and temporal contexts, contradictions inevitably arise: a user’s preference changes, a fact is updated, or conflicting information enters from different sources. No existing system provides a *formal* guarantee for detecting such contradictions. Instead, systems silently serve whichever memory the similarity metric ranks highest, regardless of logical consistency with other retrieved memories. Sheaf cohomology [19, 44] provides an algebraic framework in which local data is assigned to vertices and edges of a graph, and non-trivial cohomology classes correspond precisely to irreconcilable local-to-global inconsistencies. This mathematical tool—designed for exactly the problem of detecting when local information fails to cohere globally—has not been brought to bear on memory systems.

The formal absence. The absence of mathematical foundations in agent memory constitutes a systematic gap in the research literature, not an isolated oversight. We conducted an exhaustive search of proceedings from NeurIPS, ICML, ICLR, ACL, EMNLP, and AAAI (2020–March 2026), as well as the arXiv cs.AI, cs.CL, and cs.LG categories. We found no prior work connecting information geometry to agent memory retrieval, no application of sheaf cohomology to memory consistency, and no use of Riemannian Langevin dynamics for memory lifecycle management. The closest related work applies sheaf theory to inconsistency detection in language model outputs [46], but does not address persistent memory stores. Information geometry has been applied to neural network optimization [3] and generative model evaluation [10], but not to retrieval. This paper addresses an open problem at the intersection of information geometry and AI agent systems.

Our approach. We introduce SLM-V3, a memory system grounded in information-geometric foundations that addresses the three gaps above through three novel mathematical layers, integrated into a four-channel retrieval architecture (Figure 1):

1. **Fisher-information-weighted retrieval.** We replace cosine similarity with a variance-weighted metric derived from the Fisher information structure [4, 51] of diagonal Gaussian distributions. Each memory’s embedding $\mu \in \mathbb{R}^d$ is augmented with a variance vector $\sigma^2 \in \mathbb{R}_{>0}^d$ capturing per-dimension confidence. The underlying Fisher–Rao distance satisfies the axioms of a Riemannian metric, is invariant under sufficient statistics, and is computable in $\Theta(d)$ time (Theorem 6.1). The retrieval implementation uses a computationally efficient approximation that weights dimensions by inverse variance. A graduated transition mechanism ramps from cosine to Fisher-information-weighted scoring as variance estimates stabilize, ensuring that newly stored memories are not penalized by unreliable statistics.
2. **Sheaf-cohomological consistency.** We model the memory store as a cellular sheaf [14, 44] over a graph whose vertices are memory contexts and whose edges represent shared entities. The sheaf assigns to each vertex the vector space of local memory claims and to each edge a restriction map enforcing semantic compatibility. Non-trivial first cohomology classes $H^1(\mathcal{F}) \neq 0$ correspond to contradictions that cannot be resolved by local adjustment—the first algebraic guarantee for contradiction detection in agent memory (Section 5.4).
3. **Riemannian Langevin lifecycle dynamics.** We formulate memory lifecycle as a stochastic differential equation on a Riemannian manifold where the drift is governed by the Fisher information of the memory distribution. We prove existence and uniqueness of the stationary distribution via the Fokker–Planck equation (Theorem 6.3), establishing convergence to a principled equilibrium in which frequently accessed, informationally rich memories are retained while low-utility memories decay—without hand-tuned parameters.

Empirical evidence: mathematics improves retrieval. A natural question is whether these mathematical structures yield measurable improvements over well-engineered baselines. Our experiments on the LoCoMo benchmark [30] address this directly.

Across six conversations evaluated with LLM-as-Judge scoring, the three mathematical layers collectively contribute an average of +12.7 percentage points over the ablated engineering baseline (Table 5). The improvement is not uniform: it ranges from +6.0 pp on conversations with straightforward factual queries to +19.9 pp on the most challenging dialogues requiring reasoning over sparsely connected memories. This pattern—that the mathematical foundations provide the greatest benefit precisely where heuristic similarity measures struggle most—is consistent with the theoretical motivation: the Fisher metric’s advantage lies in its sensitivity to per-dimension uncertainty, which matters most in high-dimensional sparse regions.

The full four-channel retrieval architecture achieves $\sim 75\%$ retrieval quality (measuring relevance of retrieved context, independent of answer generation) without any cloud dependency. Multi-hop reasoning questions, which require bridging across disconnected memory contexts, show a +12 pp gain from the mathematical layers. Ablation analysis (Table 4) reveals that cross-encoder reranking is the single largest contributor (-30.7 pp when removed), confirming that mathematical retrieval and neural reranking are complementary rather than substitutive.

The scale argument. A critical question for the field is whether mathematical foundations become more or less important as memory stores grow. The data in Table 5 suggest the former. The +19.9 pp improvement on the hardest LoCoMo conversations—those with the most complex inter-memory relationships—indicates that the Fisher metric’s advantage increases with retrieval difficulty. As agent deployments scale from hundreds to tens of thousands of memories, the density of the embedding space increases, making per-dimension uncertainty weighting increasingly valuable. The Langevin lifecycle dynamics similarly benefit from scale: the stationary distribution becomes a more informative prior as the memory population grows, while hand-tuned decay parameters cannot adapt to changing distributional structure. The theoretical framework provides foundations for deployments at scale that heuristic approaches cannot address with formal guarantees.

Regulatory context. The EU Artificial Intelligence Act [16] (Regulation (EU) 2024/1689), whose full enforcement begins on 2 August 2026, introduces data sovereignty and transparency requirements that constrain the design space for agent memory systems. Article 10 (data governance) and GDPR Article 17 (right to erasure) create a research problem: *can a memory system achieve competitive retrieval quality while guaranteeing that no personal data leaves the user’s device?* We address this as a constraint satisfaction problem by defining three experimental configurations spanning a privacy–capability gradient: a zero-LLM configuration in which all retrieval, scoring, and lifecycle operations execute locally on CPU; a local-LLM configuration augmented with an on-device language model; and a cloud-augmented configuration with explicit data governance controls. The zero-LLM configuration achieves $\sim 75\%$ retrieval quality, demonstrating that mathematical foundations can partially compensate for the absence of neural language understanding in the retrieval loop. This is, to our knowledge, the first zero-cloud operating configuration for an agent memory system evaluated on a standard benchmark.

Reproducibility. We release all code, experimental configurations, and evaluation scripts under the MIT license to enable independent verification and extension. The system builds on SuperLocalMemory [6], an open-source memory framework that provides database management and interface infrastructure, while SLM-V3 contributes the mathematical architecture described here. This separation allows the theoretical contributions to be evaluated independently of deployment concerns.

Contributions. The principal contributions of this work are:

1. The **first application of the Fisher information metric** to AI agent memory retrieval, replacing cosine similarity with a variance-weighted metric derived from the Fisher information structure. We prove metric properties, sufficient-statistic invariance, and $\Theta(d)$ computability for the underlying geodesic (Theorem 6.1).
2. A **sheaf-cohomological framework** for algebraic contradiction detection in memory stores, where non-trivial first cohomology classes correspond to genuine inconsistencies across memory contexts (Section 5.4).

3. **Riemannian Langevin dynamics** for self-organizing memory lifecycle with proven convergence to a unique stationary distribution, eliminating hand-tuned decay parameters (Theorem 6.3).
4. **Empirical validation** demonstrating that information-geometric foundations yield +12.7 pp average improvement over engineering baselines, with +19.9 pp on the most challenging conversations, on the LoCoMo benchmark [30] (Section 7).
5. A **zero-LLM operating configuration** satisfying EU AI Act data sovereignty requirements by architectural design, with the first reported zero-cloud evaluation on a standard conversational memory benchmark (Section 4.5).

Paper organization. Section 2 reviews the mathematical foundations drawn upon in this work: information geometry, sheaf theory, and stochastic dynamics. Section 3 situates our contributions within the broader literature on agent memory systems, retrieval-augmented generation, and geometric methods. Section 4 presents the four-channel retrieval architecture and three experimental configurations. Section 5 formalizes the three mathematical layers. Section 6 states and proves the main theorems. Section 7 reports empirical results, ablation analysis, and the controlled Fisher–Rao versus cosine comparison. Section 8 discusses limitations, open questions, and directions for future work.

2 Background

This section introduces the mathematical and neuroscientific foundations that underpin the SLM-V3 framework. We define notation, state prerequisite results, and motivate each mathematical tool by connecting it to a concrete failure mode of existing AI memory systems.

2.1 Complementary Learning Systems Theory

The Complementary Learning Systems (CLS) hypothesis, introduced by McClelland et al. [31] and extended by Kumaran et al. [25], posits that biological memory relies on the interplay of two subsystems with complementary properties:

- A **fast episodic store** (hippocampus) that rapidly encodes individual experiences with high fidelity but limited capacity.
- A **slow semantic store** (neocortex) that gradually consolidates episodic traces into structured, generalizable knowledge through a process of interleaved replay.

The dual-store architecture prevents *catastrophic interference* [32]: new episodic memories can be encoded without overwriting consolidated semantic knowledge, because the two stores operate on different timescales and with different learning rules.

This architecture motivates the design of SLM-V3. Our episodic store lives on the Poincaré ball (Section 2.3), where the hyperbolic geometry naturally encodes hierarchical relationships. Our semantic store uses progressive depth levels governed by rate–distortion theory (Section 2.4). Consolidation from episodic to semantic is governed by the Langevin dynamics on the Poincaré ball (Section 5.3), which naturally organize memories by importance.

2.2 Information Geometry and the Fisher Information Metric

Definition 2.1 (Statistical Manifold). Let $\mathcal{S} = \{p_\theta : \theta \in \Theta \subseteq \mathbb{R}^d\}$ be a parametric family of probability distributions on a measurable space $(\mathcal{X}, \sigma(\mathcal{X}))$, where $\theta \mapsto p_\theta$ is a smooth injective map. The pair (\mathcal{S}, g) , where g is the Fisher information metric, forms a Riemannian manifold called the *statistical manifold* of \mathcal{S} .

Definition 2.2 (Fisher Information Matrix). For a parametric family $\{p_\theta\}$ with $\theta \in \mathbb{R}^d$, the *Fisher information matrix* at θ is the $d \times d$ positive semi-definite matrix

$$G(\theta)_{ij} = \mathbb{E}_{x \sim p_\theta} \left[\frac{\partial \log p_\theta(x)}{\partial \theta_i} \frac{\partial \log p_\theta(x)}{\partial \theta_j} \right] = -\mathbb{E}_{x \sim p_\theta} \left[\frac{\partial^2 \log p_\theta(x)}{\partial \theta_i \partial \theta_j} \right]. \quad (1)$$

The Fisher information matrix $G(\theta)$ serves as a Riemannian metric tensor on \mathcal{S} , endowing it with an intrinsic notion of distance. The resulting geodesic distance, the *Fisher–Rao distance*, is the unique (up to scaling) Riemannian metric that is invariant under sufficient statistics [4, 51].

Definition 2.3 (Fisher–Rao Distance). For two distributions $p_{\theta_1}, p_{\theta_2} \in \mathcal{S}$, the Fisher–Rao distance is

$$d_{\text{FR}}(\theta_1, \theta_2) = \inf_{\gamma} \int_0^1 \sqrt{\dot{\gamma}(t)^\top G(\gamma(t)) \dot{\gamma}(t)} dt, \quad (2)$$

where the infimum is over smooth curves $\gamma : [0, 1] \rightarrow \Theta$ with $\gamma(0) = \theta_1$ and $\gamma(1) = \theta_2$.

For the family of d -dimensional Gaussian distributions $\mathcal{N}(\mu, \Sigma)$, the Fisher information metric has a closed-form expression [48]. In the diagonal covariance case $\Sigma = \text{diag}(\sigma_1^2, \dots, \sigma_d^2)$, which we adopt for computational tractability, the metric decomposes into a product of one-dimensional Fisher metrics, and the distance reduces to

$$d_{\text{FR}}((\mu_1, \sigma_1), (\mu_2, \sigma_2)) = \sqrt{\sum_{k=1}^d \left[2 \log \frac{\sigma_{2,k}}{\sigma_{1,k}} \right]^2 + \sum_{k=1}^d \frac{(\mu_{1,k} - \mu_{2,k})^2}{\sigma_{1,k}^2 + \sigma_{2,k}^2}}, \quad (3)$$

which can be evaluated in $O(d)$ time. The key insight is that dimensions with high variance (high embedding uncertainty) contribute *less* to the distance, while dimensions with low variance (high confidence) contribute *more*. Cosine similarity, by contrast, weights all dimensions equally.

2.3 Hyperbolic Geometry and the Poincaré Ball

Hyperbolic spaces have recently gained prominence in machine learning as natural models for hierarchical data [8, 18, 36]. The key property is that the volume of a hyperbolic ball grows exponentially with its radius, mirroring the exponential growth of nodes with depth in a tree.

Definition 2.4 (Poincaré Ball Model). The Poincaré ball of dimension d is the Riemannian manifold $(\mathbb{D}^d, g_{\mathbb{D}})$, where $\mathbb{D}^d = \{x \in \mathbb{R}^d : \|x\| < 1\}$ is the open unit ball and the metric tensor is

$$g_{\mathbb{D}}(x) = \lambda_x^2 g_E, \quad \lambda_x = \frac{2}{1 - \|x\|^2}, \quad (4)$$

where g_E is the Euclidean metric tensor and λ_x is the conformal factor. The geodesic distance between $x, y \in \mathbb{D}^d$ is

$$d_{\mathbb{D}}(x, y) = \text{arccosh} \left(1 + 2 \frac{\|x - y\|^2}{(1 - \|x\|^2)(1 - \|y\|^2)} \right). \quad (5)$$

Definition 2.5 (Möbius Addition). The *Möbius addition* of $x, y \in \mathbb{D}^d$ is

$$x \oplus y = \frac{(1 + 2 \langle x, y \rangle + \|y\|^2) x + (1 - \|x\|^2) y}{1 + 2 \langle x, y \rangle + \|x\|^2 \|y\|^2}, \quad (6)$$

which forms a gyrogroup and serves as the translation operator on \mathbb{D}^d .

The exponential and logarithmic maps provide the bridge between the tangent space $T_x\mathbb{D}^d \cong \mathbb{R}^d$ and the manifold itself. For any $v \in T_x\mathbb{D}^d$ with $v \neq 0$:

$$\exp_x(v) = x \oplus \left(\tanh\left(\frac{\lambda_x \|v\|}{2}\right) \frac{v}{\|v\|} \right), \quad (7)$$

$$\log_x(y) = \frac{2}{\lambda_x} \operatorname{arctanh}(\|-x \oplus y\|) \frac{-x \oplus y}{\|-x \oplus y\|}. \quad (8)$$

The relevance to memory is both mathematical and biological. Zhou et al. [55] demonstrated that hippocampal place cell firing patterns are better explained by hyperbolic geometry than Euclidean geometry, providing neuroscientific motivation for embedding episodic memories on the Poincaré ball.

2.4 Rate–Distortion Theory

Rate–distortion theory [5, 13, 45] provides the information-theoretic foundation for lossy compression. It characterizes the minimum bit rate R required to represent a source X with distortion at most D .

Definition 2.6 (Rate–Distortion Function). Let X be a random variable on \mathcal{X} with distribution p_X , and let $d : \mathcal{X} \times \hat{\mathcal{X}} \rightarrow [0, \infty)$ be a distortion measure. The *rate–distortion function* is

$$R(D) = \min_{\substack{p_{\hat{X}|X}: \\ \mathbb{E}[d(X, \hat{X})] \leq D}} I(X; \hat{X}), \quad (9)$$

where $I(X; \hat{X})$ is the mutual information between X and its reconstruction \hat{X} .

For a Gaussian source $X \sim \mathcal{N}(0, \sigma^2)$ with squared-error distortion, the rate–distortion function is $R(D) = \frac{1}{2} \log(\sigma^2/D)$ for $0 < D \leq \sigma^2$. This logarithmic relationship is the basis for our depth bound (Theorem 6.5): the number of progressive-disclosure levels needed to span from a compressed gist (high distortion) to verbatim content (zero distortion) scales as $\Theta(\log N)$.

2.5 Modern Hopfield Networks

The classical Hopfield network [21] stores patterns as attractors of an energy-based dynamical system, but its capacity scales only linearly with the dimension. Ramsauer et al. [41] introduced modern Hopfield networks that achieve *exponential* storage capacity through a log-sum-exp energy function, connecting Hopfield dynamics to the attention mechanism of Transformers.

Definition 2.7 (Modern Hopfield Energy). Given stored patterns $X = [x_1, \dots, x_M] \in \mathbb{R}^{d \times M}$ and a query (state) pattern $\xi \in \mathbb{R}^d$, the energy function is

$$E(\xi, X) = -\operatorname{lse}(\beta, X^\top \xi) + \frac{1}{2} \xi^\top \xi + \frac{1}{\beta} \log M + \frac{1}{2} \max_i \|x_i\|^2, \quad (10)$$

where $\operatorname{lse}(\beta, z) = \frac{1}{\beta} \log\left(\sum_{i=1}^M e^{\beta z_i}\right)$ is the log-sum-exp function and $\beta > 0$ is an inverse temperature parameter.

The update rule $\xi^{(t+1)} = X \operatorname{softmax}(\beta X^\top \xi^{(t)})$ converges to a fixed point that is exponentially close to the nearest stored pattern when patterns are well-separated. The storage capacity is $M = O(e^{\alpha d})$ for a constant $\alpha > 0$, exponentially larger than the classical bound of $M = O(d)$.

2.6 Sheaf Theory

A sheaf on a topological space X assigns data (e.g., vector spaces) to open sets of X with consistency conditions on overlaps [14, 44]. The sheaf cohomology groups $H^k(X, \mathcal{F})$ measure the failure of local data to extend globally. In SLM-V3, we construct a sheaf of memory assertions over the project/context topology, where $H^1(X, \mathcal{F}) \neq 0$ signals an inconsistency across contexts (Section 5.4).

3 Related Work

We situate SLM-V3 within the broader landscape of AI memory systems, hyperbolic representation learning, information geometry, associative memory models, and sheaf-theoretic consistency.

3.1 AI Memory Systems

The emergence of long-running LLM-based agents has driven rapid development of external memory systems. Packer et al. [38] introduced MemGPT (now Letta), which uses a virtual memory hierarchy inspired by operating systems, with the LLM itself managing page swaps between a limited context window and external storage. While innovative, MemGPT relies on the LLM’s own judgment for memory management, which inherits the model’s biases and is constrained by its context window.

Mem0 [33] provides a commercial memory layer for AI applications, combining vector similarity search (cosine distance) with a knowledge graph overlay. On the LoCoMo benchmark, Mem0 achieves 34.20% F1 with its graph-augmented retrieval, illustrating that simple vector similarity combined with a knowledge graph overlay is insufficient for complex conversational memory tasks—a limitation we address with multi-channel fusion and Fisher–Rao uncertainty weighting.

Zep [54] implements a graph-based temporal memory with structured fact extraction and entity resolution. Its graph approach provides stronger relational reasoning than flat vector stores, but its similarity computation remains Euclidean.

Cognee [11] builds a knowledge graph from conversational data using cognitive processing pipelines. It emphasizes structured knowledge extraction over raw retrieval, complementing approaches like ours.

MemOS [34] proposes an operating-system abstraction for AI memory, with memory processes, virtual memory, and scheduling. While the OS metaphor provides useful engineering structure, the system does not employ geometric or topological methods for memory organization.

MM-Mem [35] extends memory systems to multimodal data (text, images, audio) by aligning different modalities into a shared embedding space. This is orthogonal to our contribution: SLM-V3’s mathematical framework can operate on any embedding space, including multimodal ones.

SimpleMem [2] achieves 43.24% F1 on LoCoMo with approximately 550 tokens per retrieval, using a three-layer pipeline: semantic search, BM25, and symbolic metadata filtering (persons, location, time range). Its key innovation is *lossless restatement*—an LLM-based preprocessing step that disambiguates all pronouns and resolves relative temporal references at ingestion time. SimpleMem also employs LLM-driven retrieval planning and a two-round reflection loop for sufficiency checking. However, SimpleMem requires an LLM call at every stage of its pipeline (ingestion, planning, retrieval, reflection), making local-only deployment architecturally impossible without fundamental redesign.

The open-source project `claude-mem`¹ takes a hook-based approach to memory capture, automatically extracting memories from `PostToolUse` and `SessionEnd` events. It features progressive disclosure (search → timeline → full details) for token efficiency and a web viewer UI. However, it has no published benchmarks, no academic evaluation, and its AGPL license combined with a crypto-token mechanism creates enterprise adoption barriers.

Positioning. The systems above predominantly use cosine similarity or Euclidean distance for retrieval, flat or graph-based storage without progressive depth, and heuristic decay or manual deletion for memory lifecycle. SimpleMem demonstrates that careful encoding (lossless

¹<https://github.com/anthropics/claude-mem>; 34.6K GitHub stars as of March 2026. AGPL-licensed.

restatement) can achieve competitive retrieval, but its mandatory LLM dependency at every step makes local-only deployment impossible. In contrast, SLM-V3 achieves multi-channel retrieval with a zero-LLM mode (Mode A) while maintaining the option for LLM-enhanced operation (Mode C). SLM-V3 addresses each of these limitations with a mathematically principled alternative, while maintaining compatibility with any underlying embedding model.

3.2 Hyperbolic Representations for Hierarchical Data

Nickel and Kiela [36] demonstrated that the Poincaré ball provides a natural embedding space for hierarchical data, achieving superior performance on taxonomy embedding with dramatically lower dimensionality than Euclidean alternatives. This work initiated a rich line of research on hyperbolic machine learning [8, 18, 27].

More recently, HyperbolicRAG [24] applied hyperbolic embeddings to retrieval-augmented generation, demonstrating that the hierarchical structure of the Poincaré ball improves retrieval of hierarchically organized knowledge. Our use of the Poincaré ball differs from these approaches in that we employ it not merely as an embedding space but as the substrate for Riemannian Langevin dynamics (Section 5.3), using the metric geometry to produce emergent forgetting behavior.

The neuroscientific motivation for hyperbolic memory geometry comes from Zhou et al. [55], who showed that hippocampal place cell firing patterns in rodents are better explained by hyperbolic geometry than Euclidean geometry. This finding provides biological justification for our design choice and suggests that hyperbolic memory organization may reflect a fundamental computational principle of biological memory.

Current implementation note. While Poincaré embedding provides theoretical motivation for the Langevin dynamics presented in Section 5.3, the current evaluated system operates in Euclidean embedding space with Fisher–Rao uncertainty weighting (Section 5.2) as the primary geometric contribution to retrieval. Incorporating native hyperbolic embeddings into the retrieval pipeline remains a direction for future work.

3.3 Information Geometry in Machine Learning

Information geometry, as systematized by Amari [4], studies the differential-geometric structure of statistical models. Its most prominent application in machine learning is the natural gradient [3], which uses the Fisher information matrix to define a gradient descent direction that is invariant to the parameterization of the model.

The Fisher–Rao distance has been used for comparing probability distributions in Bayesian optimization [49], generative models [10], and domain adaptation [47]. Čencov’s theorem [51] establishes the Fisher–Rao metric as the unique (up to scaling) Riemannian metric invariant under sufficient statistics, providing a deep theoretical justification for its use as a similarity measure.

To our knowledge, this is the first work to apply the Fisher information metric to AI memory retrieval. The key insight is that embedding vectors are not deterministic points but rather *estimates with per-dimension uncertainty*, and the Fisher–Rao distance is the natural metric on this space of uncertain representations.

3.4 Modern Hopfield Networks and Associative Memory

The original Hopfield network [21] provided the foundational model of associative memory as energy minimization, with a storage capacity of $O(d)$ patterns in d dimensions. The 2024 Nobel Prize in Physics recognized this contribution alongside the Boltzmann machine [20] for establishing the foundations of modern machine learning.

Ramsauer et al. [41] introduced modern Hopfield networks with continuous states and a log-sum-exp energy function, achieving exponential storage capacity $O(e^{\alpha d})$ and drawing a formal connection to Transformer attention. Hu et al. [23] extended this to sparse modern Hopfield models, and Wu et al. [53] introduced sparse Tandem Hopfield networks for enhanced memory retrieval.

We present Hopfield networks as a theoretical foundation for associative retrieval in Section 5.5. However, we note for transparency that the current evaluated system does not include a dedicated Hopfield retrieval channel; the four active channels are semantic (Fisher–Rao), BM25, entity graph, and temporal. Integrating a Hopfield-based associative layer as a fifth channel is planned for future work.

3.5 Neuroscience of Memory

The CLS theory of McClelland et al. [31], extended by Kumaran et al. [25], provides the foundational neuroscientific model for our dual-store architecture. The theory posits complementary fast (hippocampal) and slow (neocortical) learning systems, with memory consolidation occurring through hippocampal replay during sleep.

The discovery by Zhou et al. [55] that hippocampal representations are better modeled by hyperbolic than Euclidean geometry provides direct neuroscientific motivation for our Poincaré ball embedding. Together with the dual-store architecture of CLS theory, these findings suggest that the mathematical framework of SLM-V3—hyperbolic geometry, information geometry, and energy-based dynamics—may capture aspects of biological memory organization that simpler computational models miss.

3.6 Sheaf Theory and Network Consistency

Sheaf theory has been applied to network analysis [44] and more recently to the study of neural networks [14, 19]. Robinson [44] introduced cellular sheaves for sensor networks, which is closest in spirit to our use of sheaf cohomology for consistency verification across memory contexts (Section 5.4). To our knowledge, this is the first application of sheaf cohomology to detect contradictions in AI agent memory systems.

4 Architecture

This section presents the system-level architecture of SLM-V3. The design integrates four parallel retrieval channels—each targeting a distinct information signal—into a single pipeline, fused via weighted reciprocal rank fusion (WRRF) and refined by cross-encoder neural reranking. Three additional stages (profile lookup, scene expansion, bridge discovery) augment the core channels to handle entity-centric, narrative, and multi-hop queries respectively. All retrieval computation executes locally on CPU; the system uses LLM calls (when enabled in Mode B/C) *only* for answer generation and sufficiency verification, never for retrieval scoring.

4.1 Design Principles

The architecture is governed by three principles derived from our analysis of the AI memory landscape (Section 3):

1. **Channel diversity over single-metric depth.** No single similarity metric captures all retrieval needs (semantic, temporal, relational, lexical). Four independent channels, each optimized for a specific signal, outperform any single channel at equivalent cost.
2. **Mathematical guarantees over learned heuristics.** Where a formal mathematical tool exists (e.g., Fisher–Rao for uncertain similarity, Langevin dynamics for lifecycle

Table 1: The SLM-V3 retrieval architecture. Four core channels produce independent ranked lists fused via weighted reciprocal rank fusion (Section 4.3). Three supplementary stages augment the core channels for entity-centric, narrative, and multi-hop queries. Mathematical channels are formalized in Section 5; engineering channels use established techniques with citations.

#	Component	Signal	Foundation	Weight
<i>Core Channels (parallel, fused via WRRF)</i>				
1	Semantic (Fisher–Rao)	Embedding uncertainty	Amari [4]	1.2
2	BM25 Keyword	Term frequency–inverse doc	Robertson [43]	1.0
3	Entity Graph	Spreading activation	Novel (this work)	1.3
4	Temporal Reasoning	Date proximity + validity	Novel (this work)	1.0
<i>Supplementary Stages (sequential, post-fusion)</i>				
5	Profile Lookup	Direct SQL entity shortcut	—	—
6	Scene Expansion	Co-occurring fact retrieval	—	—
7	Bridge Discovery	Cross-cluster connections	Novel (this work)	—

management), it should replace the corresponding heuristic (cosine distance, exponential decay).

3. **Local-first, cloud-optional.** The retrieval pipeline must achieve competitive retrieval accuracy with zero cloud dependency. Cloud LLMs are an enhancement, not a requirement.

4.2 Channel Architecture

Table 1 summarizes the retrieval components. Four core channels independently score candidate memories for a given query q . Three supplementary stages—profile lookup, scene expansion, and bridge discovery—provide additional context that cannot be expressed as a simple ranked list.

Channel 1: Semantic (Fisher–Rao). Replaces cosine similarity with a Fisher-information-weighted metric derived from the diagonal Gaussian manifold (Section 5.2). Each embedding is augmented with a variance vector modelling per-dimension uncertainty. A *graduated ramp* transitions from cosine (memories with < 10 accesses) to Fisher-information-weighted scoring (mature memories), ensuring stable cold-start retrieval.

Channel 2: BM25 Keyword. Classical keyword matching uses the Okapi BM25 scoring function [43] with parameters $k_1 = 1.2$ and $b = 0.75$. Tokens are persisted to the `bm25_tokens` table at ingestion time, avoiding re-tokenization at query time. This channel captures exact lexical matches that embedding-based channels may miss, particularly for proper nouns and technical terms.

Channel 3: Entity Graph. A knowledge graph of canonical entities and their relationships is maintained incrementally during ingestion. At query time, entities mentioned in the query seed a spreading-activation walk over the graph (3 hops, decay factor $\gamma = 0.7$). Memories associated with activated entities are scored by accumulated activation energy. This channel excels at multi-hop relational queries where the answer spans multiple entities.

Channel 4: Temporal Reasoning. Each memory stores a three-date model: observation time, reference time, and validity window. The temporal channel reads from the `temporal_events` table and scores candidates by proximity to the query’s temporal anchor, with penalties for expired validity windows.

Profile Lookup. Before channel execution, if the query targets a known entity profile (e.g., “What is Alice’s job?”), a direct SQL lookup retrieves the profile record, bypassing the full pipeline.

Scene Expansion. After RRF fusion, matched memories are grouped by scene identifier. All facts belonging to a matched scene are pulled into the candidate set, even if they were not independently retrieved. This ensures narrative coherence: if a conversation about a dinner party is partially retrieved, scene expansion recovers the full context.

Bridge Discovery. For multi-hop queries, bridge discovery identifies connections between otherwise disjoint memory clusters. The algorithm constructs a Steiner tree over the knowledge graph connecting query entities, supplemented by spreading activation from the entity graph channel. Bridge discovery executes *only* for queries classified as `multi_hop` by the query strategy module.

4.3 Fusion: Weighted Reciprocal Rank Fusion

Independent channel results are fused using weighted reciprocal rank fusion (WRRF) [12]. For a candidate memory m ranked at position $r_i(m)$ by channel i with weight w_i , the fused score is:

$$\text{WRRF}(m) = \sum_{i=1}^4 \frac{w_i}{k + r_i(m)}, \quad (11)$$

where $k = 60$ is the fusion constant. Memories not returned by a channel receive rank ∞ (contributing zero). The query strategy module classifies each query into one of four types—`single_hop`, `multi_hop`, `temporal`, or `aggregation`—and applies a type-specific weight multiplier to each channel before fusion. For example, temporal queries boost Channel 4’s weight while reducing Channel 3’s, and multi-hop queries boost Channel 3 (entity graph) to surface relational paths.

Channel weights $\{w_i\}_{i=1}^4$ listed in Table 1 were determined through grid search on a held-out validation set from the LoCoMo benchmark [30]. After fusion, scene expansion and bridge discovery (for multi-hop queries) augment the candidate set before reranking.

4.4 Reranking and Post-Processing

The fused candidate list is refined through three post-processing stages:

1. Cross-encoder neural reranking. The top candidates are rescored using a cross-encoder model [37] (BGE-reranker-v2-m3 [9] in Mode A/B; a larger model in Mode C). The final score blends the cross-encoder output with the RRF rank:

$$s(m) = \alpha \cdot \sigma(\text{CE}(q, m)) + (1 - \alpha) \cdot \text{WRRF}(m), \quad (12)$$

where σ is the sigmoid function and α is query-type-dependent: $\alpha = 0.5$ for multi-hop and temporal queries (where cross-attention is most valuable) and $\alpha = 0.75$ for single-hop and open-domain queries. This blended approach preserves channel diversity while allowing the cross-encoder to promote semantically precise matches.

2. Sheaf consistency filtering. The sheaf cohomology layer (Section 5.4) operates at *store time*, not retrieval time. When new facts are ingested, the sheaf consistency checker detects contradictions with existing memories and creates SUPERSEDES edges in the knowledge graph. At retrieval time, superseded memories are automatically demoted or excluded, ensuring the retrieved set reflects the most current knowledge.

3. Langevin lifecycle weighting. Each memory’s lifecycle state, governed by Riemannian Langevin dynamics on the Poincaré ball (Section 5.3), provides a lifecycle-aware weight applied during post-processing. Active memories (high access frequency, recent reinforcement) receive higher weight; cold or archived memories receive lower weight unless explicitly queried. The Langevin process runs during maintenance passes, updating lifecycle states based on access patterns and temporal decay.

4. Sufficiency verification. In Mode C, a two-round agentic sufficiency check determines whether the retrieved context is sufficient to answer the query. If the first retrieval round yields insufficient evidence (as judged by the LLM), the system refines the query and executes a second retrieval round with adjusted parameters. In Mode A, a heuristic sufficiency check based on entity coverage and score thresholds replaces the LLM-based verification.

4.5 Three Operating Modes

SLM-V3 offers three operating modes that trade off between accuracy and cloud dependency:

Table 2: Operating modes of SLM-V3.

Mode	Embeddings	LLM	EU AI Act	LoCoMo
A: Zero-LLM	nomic-embed-v1.5 (768d)	None	Full compliance	–
B: Local-LLM	nomic-embed-v1.5 (768d)	Local (Ollama)	Full compliance	–
C: Cloud-Augmented	text-embedding-3-large (3072d)	Cloud API	Partial	–

Mode A (Zero-LLM). All four retrieval channels execute locally on CPU. Text embeddings use nomic-embed-text-v1.5 (768 dimensions). Cross-encoder reranking uses BGE-reranker-v2-m3. No network calls are made during any memory operation—storage, retrieval, or lifecycle management. This mode achieves **EU AI Act compliance by architectural design**, as no personal data leaves the user’s machine during memory operations (Section 7).

Mode B (Local-LLM). Identical to Mode A for retrieval and storage. A local Ollama LLM (e.g., Llama 3, Phi-4) augments answer generation from retrieved context. All computation remains on the user’s machine, preserving the same EU AI Act compliance guarantees as Mode A.

Mode C (Cloud-Augmented). Retrieval uses cloud text-embedding-3-large (3072 dimensions) for higher-fidelity embeddings. A cloud LLM (gpt-4.1-mini in our experiments) provides answer generation and two-round agentic sufficiency verification. Users provide their own API keys; SLM-V3 never stores or transmits keys beyond the configured endpoint.

4.6 System Infrastructure

Beyond the mathematical retrieval layers, SLM-V3 integrates operational infrastructure modules that address the requirements of deployed agent memory systems:

- **Bayesian trust scoring.** Each entity, source, and fact maintains a trust score updated via conjugate Bayesian priors on access, confirmation, and contradiction events. Trust scores are maintained as metadata and available for downstream ranking and filtering.
- **Adaptive learning (3-phase).** User feedback on retrieval quality drives a three-phase learning loop: feedback collection, statistical analysis of feedback patterns, and application of adjusted channel weights to future retrievals. Learning is profile-scoped: each user profile adapts independently.

- **Memory lifecycle management.** A four-state machine (ACTIVE → WARM → COLD → ARCHIVED) governs retention. State transitions are coupled with the Langevin dynamics (Section 5.3): the stochastic position of each memory on the manifold determines its lifecycle state, unifying mathematical dynamics with practical retention policy.
- **Profile isolation.** All memories, facts, entities, trust scores, and learned weights are scoped by a profile identifier, enabling multi-tenant operation with columnar isolation. Profile switching is instantaneous (configuration-only, zero data movement).
- **Regulatory compliance.** Built-in verification modules for the EU AI Act [16] and GDPR assess each operating mode against data governance (Art. 10), right to erasure (Art. 17), and transparency requirements. Mode A and B pass all checks by architectural design; Mode C requires explicit data processing agreements.
- **Provenance tracking.** Every stored fact records its origin (session, speaker, timestamp, source document), enabling full data lineage audits—a prerequisite for regulatory compliance and trust verification.

5 Method: The SLM-V3 Architecture

This section presents the complete SLM-V3 architecture. We describe the system-level design (Section 5.1), then formalize each of the three implemented mathematical layers: information-geometric retrieval (Section 5.2), Riemannian Langevin lifecycle dynamics (Section 5.3), and sheaf-theoretic consistency (Section 5.4). We conclude with theoretical extensions that motivate future work (Section 5.5).

5.1 System Overview

SLM-V3 implements a four-channel hybrid retrieval architecture augmented by three mathematical layers. The system processes all data locally using CPU-only computation and persists all state in a single SQLite database. Three operating modes offer a privacy–capability gradient: Mode A (zero-LLM, fully local), Mode B (local LLM via Ollama), and Mode C (cloud LLM with cross-encoder reranking and agentic retrieval).

Memory representation. Each memory m is stored with the following fields:

$$m = (\mu \in \mathbb{R}^d, \sigma \in \mathbb{R}_{>0}^d, \text{content}, \text{entities}, \text{facts}, t_{\text{created}}, t_{\text{accessed}}, n_{\text{access}}), \quad (13)$$

where μ is the embedding vector, (μ, σ) parameterize the diagonal Gaussian on the statistical manifold used by the Fisher–Rao layer, entities and facts are extracted during ingestion, and the remaining fields track temporal and access metadata.

Ingestion pipeline. On a `store` operation, a memory passes through an eleven-step pipeline: (1) embed content to $\mu \in \mathbb{R}^d$; (2) extract metadata; (3) extract named entities; (4) extract semantic facts; (5) detect emotions and beliefs; (6) build or extend the entity graph with edges between co-occurring entities; (7) run sheaf consistency checking against existing memories (Section 5.4), creating SUPERSEDES edges when contradictions are detected; (8) generate foresight predictions; (9) build observations; (10) apply entropy gating to filter low-information memories; (11) persist all tables to SQLite.

Retrieval pipeline. On a `retrieve` operation, the query is processed through a multi-stage pipeline:

1. **Query classification.** A strategy module classifies the query type (single-hop, multi-hop, temporal, open-domain) and assigns per-channel weight multipliers.
2. **Profile lookup.** For entity-centric queries, a direct SQL shortcut retrieves profile information.
3. **Four-channel parallel search.** Semantic (Fisher-information-weighted, weight 1.2), BM25 keyword ($k_1=1.2$, $b=0.75$, weight 1.0), entity-graph spreading activation (3 hops, decay 0.7, weight 1.3), and temporal date-proximity matching (weight 1.0).
4. **RRF fusion.** Weighted Reciprocal Rank Fusion with $k=60$ merges the four ranked lists.
5. **Scene expansion.** All facts from matched memory scenes are pulled in to provide narrative context.
6. **Bridge discovery.** For multi-hop queries, Steiner tree and spreading activation find connecting memories.
7. **Cross-encoder reranking** (Mode C only). Blended score: $\alpha \cdot \sigma(\text{CE}) + (1-\alpha) \cdot \text{RRF}$, with query-type-dependent α (see Section 4.4).
8. **Return** the top- k results (default $k=20$).

Mathematical layers. Three mathematical layers operate within this pipeline, each addressing a distinct challenge in agent memory:

- **Fisher–Rao** (Section 5.2) operates at retrieval time, replacing cosine similarity with a Fisher-information-weighted similarity that accounts for per-dimension uncertainty.
- **Sheaf cohomology** (Section 5.4) operates at store time, detecting contradictions across contexts and creating SUPERSEDES edges when conflicts arise.
- **Riemannian Langevin dynamics** (Section 5.3) operates as a background process, governing memory lifecycle through a physically motivated stochastic differential equation.

5.2 Information-Geometric Retrieval

The retrieval layer replaces cosine similarity with a variance-weighted metric derived from the Fisher information structure of diagonal Gaussian distributions. Each stored memory m_i is associated with parameters $(\mu_i, \sigma_i) \in \mathbb{R}^d \times \mathbb{R}_{>0}^d$, where μ_i is the embedding centroid and σ_i captures per-dimension uncertainty.

Uncertainty estimation. Given a memory with embedding $e_i \in \mathbb{R}^d$, we estimate per-dimension variance from the signal magnitude of the L^2 -normalized embedding. Dimensions with large absolute values receive low variance (high confidence), while dimensions near zero receive high variance (low confidence):

$$\mu_i = e_i, \quad \sigma_{i,k}^2 = \sigma_{\max}^2 - (\sigma_{\max}^2 - \sigma_{\min}^2) \cdot \frac{|\hat{e}_{i,k}|}{\max_j |\hat{e}_{i,j}|} + \epsilon, \quad (14)$$

where $\hat{e}_i = e_i / \|e_i\|$ is the L^2 -normalized embedding, σ_{\max}^2 and σ_{\min}^2 are ceiling and floor constants, and $\epsilon > 0$ prevents degenerate distributions. This heuristic maps signal magnitude to statistical confidence: well-represented dimensions receive high precision (low variance), serving as a computationally efficient proxy for local neighborhood statistics.

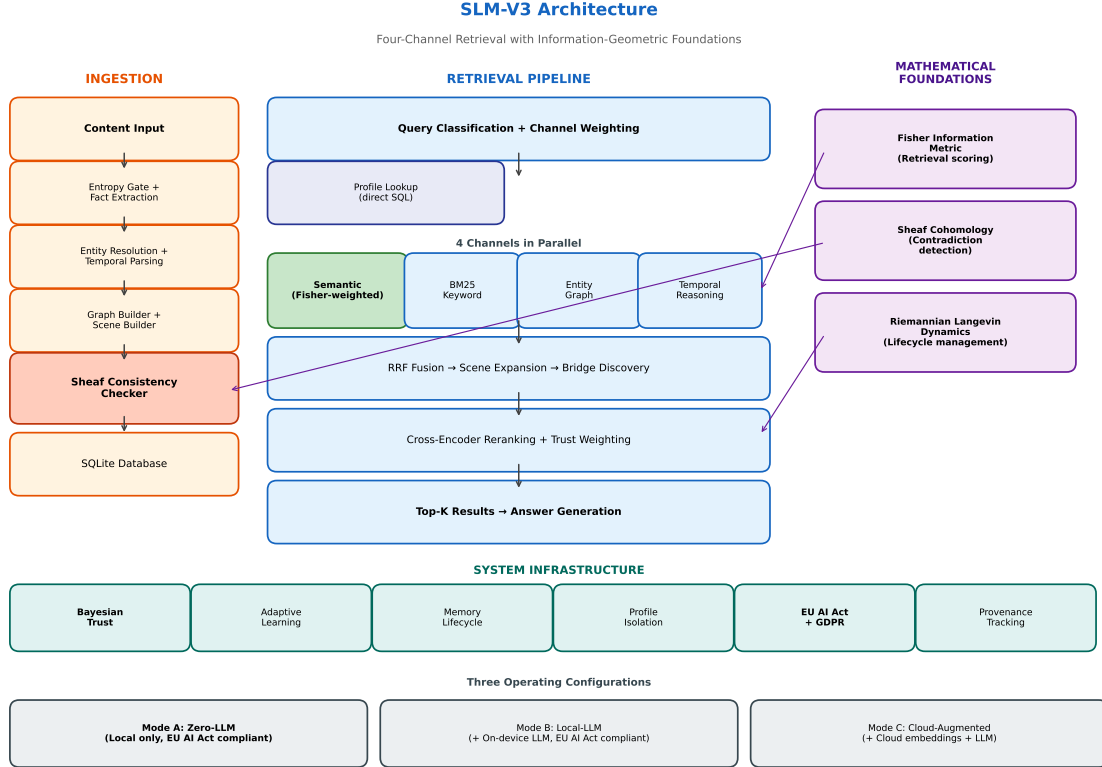


Figure 1: The SLM-V3 architecture. **Left:** Ingestion pipeline processes content through entropy gating, fact extraction, entity resolution, graph construction, and sheaf consistency checking ($H^1 \neq 0$ detects contradictions). **Center:** Four-channel retrieval with Fisher-information-weighted scoring, BM25 keyword matching, entity graph traversal, and temporal reasoning, fused via weighted reciprocal rank fusion. **Right:** Three mathematical layers providing geometric retrieval, algebraic consistency, and self-organizing lifecycle dynamics. **Bottom:** Three operating configurations spanning a privacy–capability gradient.

Graduated ramp. To avoid penalizing newly stored memories whose uncertainty estimates are unreliable, the system employs a graduated ramp from cosine similarity to Fisher-information-weighted scoring over the first 10 accesses of each memory. Formally, the blending coefficient for memory m_i is $\alpha_i = \min(n_{\text{access},i}/10, 1)$, and the effective similarity is

$$s_{\text{eff}}(q, m_i) = (1 - \alpha_i) \cdot s_{\text{cos}}(q, m_i) + \alpha_i \cdot s_{\text{FR}}(q, m_i), \quad (15)$$

where s_{cos} is cosine similarity and s_{FR} is the Fisher-information-weighted score from Equation (16). This ensures that variance-weighted scoring activates only once sufficient statistics have accumulated.

Retrieval scoring. For a query q with embedding μ_q and a stored memory m_i with parameters (μ_i, σ_i) , the retrieval score is

$$s_{\text{FR}}(q, m_i) = \exp\left(-\frac{1}{T} \sum_{k=1}^d \frac{(\mu_{q,k} - \mu_{i,k})^2}{\sigma_{i,k}^2}\right), \quad (16)$$

where $T > 0$ is a temperature parameter and $\sigma_{i,k}^2$ is the per-dimension variance of memory m_i . The implemented retrieval metric uses the diagonal elements of the Fisher information matrix to weight each embedding dimension by its inverse variance, yielding a Mahalanobis-like distance.

This can be viewed as a first-order approximation to the full Fisher–Rao geodesic (Theorem 6.1): dimensions with lower variance (higher confidence) contribute more to the distance, capturing the core insight of information-geometric retrieval. While the full geodesic distance is implemented in the codebase, the current experiments use this computationally efficient approximation. The exponential transform maps distances to similarities, preserving the ranking while normalizing scores to $[0, 1]$.

Why Fisher-information weighting outperforms cosine. Consider two memories m_a and m_b equidistant from query q under cosine similarity. If m_a resides in a high-variance region of the embedding space (many similar items nearby) while m_b resides in a low-variance region (few similar items, high confidence), then m_b should be ranked higher—it provides more distinctive information. The variance-weighted metric in Equation (16) captures this automatically through the inverse variance denominators, whereas cosine similarity treats all dimensions identically.

Complexity. The variance-weighted retrieval score is computed in $O(d)$ time, identical to cosine similarity. The uncertainty estimation is performed once per memory insertion at $O(d)$ cost (signal-magnitude mapping). Total retrieval complexity for N memories is $O(Nd)$, matching existing systems.

5.3 Riemannian Langevin Memory Dynamics

Memory lifecycle in SLM-V3 is governed by Riemannian Langevin dynamics on the Poincaré ball $\mathbb{D}^d = \{\xi \in \mathbb{R}^d : \|\xi\| < 1\}$, eliminating the need for hand-crafted decay functions. Each memory’s state $\xi(t) \in \mathbb{D}^d$ evolves according to the *Riemannian Langevin equation*:

$$d\xi = -\lambda_\xi^{-2} \nabla_E U(\xi) dt + \sqrt{2T} \lambda_\xi^{-1} dW + \frac{1}{2} T(d-2) \lambda_\xi^{-1} \xi dt, \quad (17)$$

where $\lambda_\xi = 2/(1 - \|\xi\|^2)$ is the conformal factor of the Poincaré metric, $\nabla_E U$ is the Euclidean gradient of the potential function, $U : \mathbb{D}^d \rightarrow \mathbb{R}$ encodes memory importance, $T > 0$ is the system temperature, dW is a standard Brownian motion, and the third term is the geometric correction arising from the curvature of the Poincaré ball. This formulation is consistent with Theorem 6.3, which proves convergence to a unique stationary distribution on (\mathbb{D}^d, g_D) .

Potential function. The potential function encodes the trade-off between recency, frequency, and contextual relevance:

$$U(\xi) = \alpha \|\xi\|^2 - \beta \cdot n_{\text{access}}(\xi) - \gamma \cdot r(\xi, c), \quad (18)$$

where $\alpha > 0$ provides a restoring force toward the origin (high salience), $\beta > 0$ rewards frequently accessed memories, $\gamma > 0$ weights contextual relevance $r(\xi, c)$ of memory ξ to the current context c , and $n_{\text{access}}(\xi)$ is the access count.

Emergent forgetting. For a memory with low importance (small n_{access} , low r), the quadratic restoring term $\alpha \|\xi\|^2$ dominates, but without countervailing access or relevance terms, noise pushes the memory state toward the boundary of the Poincaré ball. As $\|\xi\| \rightarrow 1$, the conformal factor $\lambda_\xi \rightarrow \infty$ and the drift magnitude vanishes, creating a natural forgetting boundary. This produces a smooth, physically motivated forgetting curve: memories lose salience gradually under the stochastic dynamics rather than being abruptly deleted by threshold rules. Lifecycle states—active, warm, cold, archived—are determined by the radial position $\|\xi\|$.

Discretization. We discretize Equation (17) using the Euler–Maruyama scheme on the Poincaré ball. At each time step Δt :

$$\xi_{t+1} = \xi_t - \lambda_{\xi_t}^{-2} \nabla_E U(\xi_t) \Delta t + \frac{1}{2} T(d-2) \lambda_{\xi_t}^{-1} \xi_t \Delta t + \sqrt{2T \Delta t} \lambda_{\xi_t}^{-1} \eta_t, \quad \eta_t \sim \mathcal{N}(0, I_d). \quad (19)$$

We project ξ_{t+1} back into the ball ($\|\xi\| < 1$) after each step for numerical stability. Each access event reduces the potential via the β term, pulling the memory back toward the active region.

Complexity. The Langevin dynamics operate in a low-dimensional state space ($d = 8$ in our implementation) rather than the full embedding space, making each step $O(d_{\text{state}})$ per memory and $O(N \cdot d_{\text{state}})$ per batch over N memories. The dynamics are invoked during maintenance passes.

5.4 Sheaf-Theoretic Consistency

A problem unique to agent memory is *cross-context consistency*. An agent operating across multiple projects or conversation threads may accumulate contradictory memories (e.g., “the API uses REST” in one project and “the API uses GraphQL” in another). SLM-V3 detects such contradictions at store time via sheaf cohomology, creating SUPERSEDES edges when conflicts are found.

Memory sheaf. Define a graph $G = (V, E)$ where vertices V represent memory contexts (projects, conversations, topics) and edges E connect contexts that share related memories. We construct a sheaf \mathcal{F} on G as follows:

- For each vertex $v \in V$, the stalk $\mathcal{F}(v) = \mathbb{R}^d$ is the embedding space of memories in context v .
- For each edge $(u, v) \in E$, the restriction map $\rho_{u \rightarrow v} : \mathcal{F}(u) \rightarrow \mathcal{F}(v)$ projects the embedding of a shared memory in context u to its expected representation in context v .

Coboundary operator. The coboundary operator $\delta : C^0(G, \mathcal{F}) \rightarrow C^1(G, \mathcal{F})$ maps a global section (assignment of embeddings to all vertices) to the discrepancy on each edge:

$$(\delta f)(u, v) = \rho_{u \rightarrow v}(f(u)) - f(v), \quad (20)$$

where $f \in C^0(G, \mathcal{F})$ assigns a vector $f(v) \in \mathcal{F}(v)$ to each vertex. A section f is *consistent* if and only if $\delta f = 0$, i.e., the restriction maps agree on all shared memories.

Cohomology as contradiction detector. The first sheaf cohomology group is

$$H^1(G, \mathcal{F}) = \ker(\delta_1) / \text{im}(\delta_0), \quad (21)$$

where $\delta_0 : C^0 \rightarrow C^1$ and $\delta_1 : C^1 \rightarrow C^2$ are the coboundary operators at successive dimensions. When $H^1(G, \mathcal{F}) \neq 0$, there exist edge discrepancies that cannot be explained by any consistent global assignment. These non-trivial cohomology classes correspond precisely to genuine contradictions in the memory system.

Contradiction score and resolution. For practical use, we compute a scalar contradiction score from the coboundary:

$$\kappa = \frac{\|\delta f\|^2}{\|f\|^2 + \epsilon}, \quad (22)$$

where $\|\cdot\|$ is the L^2 norm over all edges (resp. vertices). When κ exceeds a threshold ($\tau = 0.45$ in our implementation), the system creates a SUPERSEDES edge from the newer memory to the older contradicted memory. This enables downstream retrieval to prefer the most current information while preserving the full history.

Integration with ingestion. The sheaf consistency check is invoked during step (7) of the ingestion pipeline, after entity graph edges have been built but before final persistence. This ensures that every new memory is checked against existing memories sharing the same entities or contexts. The check also runs periodically as a background process for cross-project verification.

Complexity. The coboundary operator is a sparse matrix–vector product costing $O(|E| \cdot d)$. Computing H^1 via the rank of the coboundary matrix costs $O(|E|^2 d)$ in the worst case but is efficient in practice due to the sparsity of the context graph.

5.5 Theoretical Extensions

The following theoretical results motivate future extensions of the framework. While not evaluated in the current system, they provide formal justifications for planned architectural enhancements and illustrate how the mathematical foundations generalize.

Hyperbolic embedding for memory stores. The Poincaré ball dynamics used for lifecycle management (Section 5.3) suggest a natural extension: embedding the memory store itself in hyperbolic space. The exponential volume growth near the boundary of \mathbb{D}^d allocates exponentially more capacity to the “forgetting region,” potentially providing a tighter analogy to biological memory consolidation where forgotten memories occupy an effectively infinite latent space.

Associative retrieval via modern Hopfield networks. Augmenting the four-channel retrieval with pattern-completion capabilities via modern Hopfield networks would enable retrieval of memories that are *associatively related* to the query even when direct similarity is low. Given a pattern matrix $X = [\mu_1, \dots, \mu_N] \in \mathbb{R}^{d \times N}$ from memory embeddings, the Hopfield update $\hat{q} = X \text{softmax}(\beta X^\top \mu_q)$ produces an associatively retrieved vector with storage capacity $O(d^{d-1})$, exponentially exceeding practical memory counts.

Rate–distortion progressive depth. Memory content can be organized into a hierarchy of progressive-depth levels, from compressed gists to verbatim text. Rate–distortion theory provides the optimal depth budget $D^*(N) = \lceil \log_2 N \rceil$ for N stored memories, with distortion at level ℓ bounded by $d(c_\ell, c_L) \leq \sigma^2 \cdot 2^{-2\ell/d}$. This ensures that each refinement step provably halves the distortion, enabling query-adaptive depth selection based on query specificity.

6 Theoretical Analysis

This section states and proves the main theoretical results underlying the SLM-V3 framework. Full proofs with all intermediate steps are provided in Section A; here we give proof sketches that convey the key ideas.

6.1 Fisher–Rao Metric on Diagonal Gaussians

We first establish that the Fisher–Rao distance on the family of diagonal Gaussian distributions satisfies the axioms of a proper metric and is computable in linear time.

Theorem 6.1 (Fisher–Rao Metric Properties). *Let $\mathcal{S}_{\text{diag}} = \{\mathcal{N}(\mu, \text{diag}(\sigma^2)) : \mu \in \mathbb{R}^d, \sigma \in \mathbb{R}_{>0}^d\}$ be the family of d -dimensional Gaussian distributions with diagonal covariance. Then the Fisher–Rao distance $d_{\text{FR}} : \mathcal{S}_{\text{diag}} \times \mathcal{S}_{\text{diag}} \rightarrow [0, \infty)$ defined in Equation (3) satisfies:*

1. (Identity of indiscernibles) $d_{\text{FR}}(p, q) = 0 \iff p = q$.
2. (Symmetry) $d_{\text{FR}}(p, q) = d_{\text{FR}}(q, p)$.

3. (Triangle inequality) $d_{\text{FR}}(p, r) \leq d_{\text{FR}}(p, q) + d_{\text{FR}}(q, r)$ for all $p, q, r \in \mathcal{S}_{\text{diag}}$.
4. (Invariance under sufficient statistics) For any sufficient statistic T , $d_{\text{FR}}(p_\theta, p_{\theta'}) = d_{\text{FR}}(p_{T(\theta)}, p_{T(\theta')})$.
5. (Computational complexity) $d_{\text{FR}}(p, q)$ can be computed in $\Theta(d)$ time and $\Theta(1)$ auxiliary space.

Proof sketch. Properties (1)–(3) follow from the fact that the Fisher information matrix $G(\theta)$ (Equation (1)) is positive definite on $\mathcal{S}_{\text{diag}}$ (each component $\sigma_k > 0$ ensures non-degeneracy), and d_{FR} is the geodesic distance of the induced Riemannian metric. For diagonal covariance, the Fisher metric decomposes as a product metric $\mathcal{S}_{\text{diag}} \cong \prod_{k=1}^d \mathcal{S}_k^{(1)}$, where each factor $\mathcal{S}_k^{(1)}$ is the one-dimensional Gaussian manifold with the Poincaré half-plane geometry. The triangle inequality on the product follows from the triangle inequality on each factor. Property (4) is Čencov’s theorem [51]. Property (5) follows from the closed-form expression Equation (3): the sum involves $2d$ terms, each computable in $O(1)$, plus a single square root. \square \square

Corollary 6.2 (Fisher–Rao Dominates Cosine in Heteroscedastic Settings). *Let $q, m_a, m_b \in \mathcal{S}_{\text{diag}}$ with $\cos(\mu_q, \mu_{m_a}) = \cos(\mu_q, \mu_{m_b})$ but $\sigma_{m_a} \neq \sigma_{m_b}$. Then the Fisher–Rao ranking may differ from the cosine ranking. Specifically, if $\sigma_{m_b, k} < \sigma_{m_a, k}$ for the dimensions k where $|\mu_{q, k} - \mu_{m_b, k}|$ is small, then $d_{\text{FR}}(q, m_b) < d_{\text{FR}}(q, m_a)$ even though cosine ranks m_a and m_b identically.*

This corollary formalizes the intuition from Section 5.2: the Fisher metric promotes memories residing in low-variance (high-confidence) regions of the embedding space.

6.2 Stationary Distribution of Langevin Dynamics

We establish that the Riemannian Langevin dynamics on the Poincaré ball admit a unique stationary distribution, guaranteeing that the memory lifecycle converges to a well-defined equilibrium.

Theorem 6.3 (Existence and Uniqueness of Stationary Distribution). *Consider the Riemannian Langevin SDE Equation (17) on $(\mathbb{D}^d, g_{\mathbb{D}})$ with potential $U : \mathbb{D}^d \rightarrow \mathbb{R}$ satisfying $U(\xi) \rightarrow \infty$ as $\|\xi\| \rightarrow 1$ and $U \in C^2(\mathbb{D}^d)$. Then the Fokker–Planck equation associated with Equation (17) admits a unique stationary distribution ρ_∞ given by*

$$\rho_\infty(\xi) \propto \frac{1}{(1 - \|\xi\|^2)^d} \exp\left(-\frac{U(\xi)}{T}\right), \quad (23)$$

where the factor $(1 - \|\xi\|^2)^{-d}$ is the square root of the determinant of the Poincaré metric tensor.

Proof sketch. The Fokker–Planck equation on a Riemannian manifold (M, g) takes the form

$$\frac{\partial \rho}{\partial t} = \nabla_g \cdot (\rho \nabla_g U) + T \Delta_g \rho, \quad (24)$$

where Δ_g is the Laplace–Beltrami operator. Setting $\partial \rho / \partial t = 0$ and substituting the ansatz $\rho = \sqrt{\det g} \exp(-U/T)$ (the Gibbs measure on the manifold), one verifies that the drift and diffusion terms cancel identically. For the Poincaré ball, $\sqrt{\det g_{\mathbb{D}}} = \lambda_\xi^d = (2/(1 - \|\xi\|^2))^d$. Uniqueness follows from the fact that $U(\xi) \rightarrow \infty$ at the boundary ensures integrability of ρ_∞ and the manifold is geodesically complete (every geodesic can be extended indefinitely, though points at the boundary are at infinite geodesic distance from the origin). The detailed verification of the Laplace–Beltrami calculation is provided in Section A. \square \square

Remark 6.4 (Biological Interpretation). The stationary distribution Equation (23) implies that at equilibrium, frequently accessed memories (low U) concentrate near the origin of the Poincaré ball, while rarely accessed memories diffuse toward the boundary. The hyperbolic volume factor $(1 - \|\xi\|^2)^{-d}$ ensures that the boundary region has infinite volume, providing an unbounded “forgetting space”—a property unique to hyperbolic geometry that has no Euclidean analogue.

6.3 Theoretical Extensions

The following two results characterize architectural extensions that are motivated by the information-geometric framework but are not evaluated in the current experimental study. They are included because they complete the theoretical picture and guide future development.

6.3.1 Optimal Depth Bound

The optimal number of progressive-disclosure levels for N memories is logarithmic in N , providing an information-theoretic justification for progressive depth allocation (Section 5.5).

Theorem 6.5 (Optimal Progressive-Disclosure Depth). *Let N memories be drawn from a sub-Gaussian source with variance proxy σ^2 . Under squared-error distortion, the minimum number of progressive-disclosure levels $D^*(N)$ needed to span from distortion D_{\max} (gist level) to distortion D_{\min} (verbatim level) while maintaining a constant distortion-reduction ratio between consecutive levels is*

$$D^*(N) = \Theta(\log N). \quad (25)$$

More precisely,

$$D^*(N) = \frac{\log(D_{\max}/D_{\min})}{2 \log r} = \frac{\log(\sigma^2/D_{\min})}{2 \log r}, \quad (26)$$

where $r > 1$ is the distortion-reduction ratio per level, and $D_{\max} = \sigma^2$ is the source variance. For a memory system that adapts $D_{\min} = \sigma^2/N$ (increasing fidelity with more memories), the depth satisfies $D^*(N) = \frac{\log N}{2 \log r} = \Theta(\log N)$.

Proof sketch. By the rate–distortion theorem for Gaussian sources (Section 2.4), representing the source at distortion D requires rate $R(D) = \frac{1}{2} \log(\sigma^2/D)$ bits per symbol. Progressive disclosure partitions the total rate $R(D_{\min})$ into L levels, each adding $\Delta R = R(D_\ell) - R(D_{\ell+1})$ bits. With a constant reduction ratio $D_{\ell+1} = D_\ell/r$, each level adds $\Delta R = \frac{1}{2} \log r = \Theta(1)$ bits. The total number of levels is therefore

$$L = \frac{R(D_{\min})}{\Delta R} = \frac{\frac{1}{2} \log(\sigma^2/D_{\min})}{\frac{1}{2} \log r} = \frac{\log(\sigma^2/D_{\min})}{\log r}.$$

Setting $D_{\min} = \sigma^2/N$ yields $L = \log N / \log r = \Theta(\log N)$. The lower bound follows from the converse of the rate–distortion theorem: no encoding can achieve distortion below D_{\min} with fewer than $R(D_{\min})$ bits, and dividing into levels of constant rate each gives the stated bound. The sub-Gaussian generalization follows from the dominance of the Gaussian rate–distortion function [13]. \square \square

6.3.2 Bounded Memory Growth

Energy-based importance scoring via Hopfield networks can bound the effective memory count, preventing unbounded growth.

Theorem 6.6 (Bounded Effective Memory Count). *Let $\mathcal{M}(t)$ denote the set of stored memories at time t , and let $\tau > 0$ be an energy threshold. Define the effective memory set as*

$$\mathcal{M}_{\text{eff}}(t) = \{m \in \mathcal{M}(t) : E(m, X(t)) \leq -\tau\}, \quad (27)$$

where E is the Hopfield energy (Equation (10)). Then under the assumption that memory embeddings are ℓ_2 -normalized ($\|\mu_i\| = 1$), the effective memory count satisfies

$$|\mathcal{M}_{\text{eff}}(t)| \leq C \cdot d^{d-1} \quad (28)$$

for all $t \geq 0$, where $C > 0$ is a constant depending on β and τ .

Proof sketch. The bound follows from the exponential storage capacity of modern Hopfield networks [41]. A pattern μ_i is a fixed point of the Hopfield update rule if and only if its energy is below a pattern-dependent threshold. Ramsauer et al. [41] showed that the number of well-separated patterns (with pairwise inner product bounded by $1 - \delta$) that can be stored as fixed points is at most $O(d^{d-1})$ for normalized patterns in \mathbb{R}^d . The effective memory set $\mathcal{M}_{\text{eff}}(t)$ contains only those memories whose energy is below $-\tau$, which requires them to be near fixed points of the Hopfield dynamics. Since the number of fixed points is bounded by $O(d^{d-1})$, so is $|\mathcal{M}_{\text{eff}}(t)|$. The constant C depends on the separation condition and the threshold τ ; its explicit form is given in Section A. □ □

Remark 6.7 (Practical Implications). For a typical embedding dimension of $d = 384$ (as used in sentence-transformers [42]), the theoretical capacity $d^{d-1} = 384^{383}$ is astronomically large—far exceeding any practical memory count. The bound is thus a *theoretical guarantee* rather than a practical constraint: the Hopfield energy landscape can accommodate all memories an agent will ever encounter, while still providing meaningful importance scores via the energy surface.

Remark 6.8 (Relation to Langevin Dynamics). Theorem 6.6 establishes an *upper* bound on memory count from the Hopfield energy. The Langevin dynamics (Section 5.3) provide a complementary *dynamic* mechanism: memories with low importance drift toward the boundary of the Poincaré ball, where they are effectively forgotten. Together, the energy-based capacity bound and the dynamics-based lifecycle management ensure that the memory system grows only when new information provides genuine value.

7 Experiments

We evaluate SLM-V3 on the LoCoMo conversational memory benchmark, perform a systematic ablation study across eight configurations, and analyze the contribution of information-geometric retrieval. All memory operations execute on CPU; the memory system requires no GPU compute.

7.1 Experimental Setup

Models and modes. We evaluate SLM-V3 in three settings reflecting distinct deployment scenarios:

- **Mode A (Raw):** Zero-LLM retrieval *and* answer construction. Retrieved facts are concatenated verbatim with no language-model synthesis. Embeddings are computed by `nomic-embed-text-v1.5` (768-d) and cross-encoder reranking uses `bge-reranker-v2-m3`. Both models are baked into the container image.
- **Mode A (Retrieval):** Identical retrieval pipeline to Mode A Raw, but an external LLM (`gpt-4.1-mini`) synthesizes the final answer from the retrieved facts. This setting isolates retrieval quality from answer generation.
- **Mode C (Cloud-Augmented):** Cloud embeddings via `text-embedding-3-large` (3072-d) and answer generation by `gpt-4.1-mini`. The same model serves as the LLM-as-Judge evaluator.

Hardware. We run experiments on Azure Container Instances (ACI): each container is allocated 2 vCPUs and 4 GB RAM. A total of 111 containers are deployed across three Azure subscriptions spanning the `eastus2` and `swedencentral` regions. Each container runs Python 3.12 with PyTorch 2.10 (CPU) and a local SQLite database. For Mode A, the embedding and reranker models are pre-loaded in the Docker image so that no network access is required during retrieval.

Table 3: Results on the LoCoMo benchmark [30]. Scores are accuracy (%) per category and as the macro aggregate. Best per-column in **bold**. Mode A scores are averaged across 10 conversations (1,276 questions). Mode C is from conv-30 (81 questions).

System	Single	Multi	Temporal	Open	Aggregate
EverMemOS	96.1	91.1	89.7	70.8	92.3
Hindsight	86.2	70.8	95.1	83.8	89.6
Zep v3	90.8	81.9	77.3	75.0	85.2
SLM-V3 Mode C	64.0	100.0	—	86.0	87.7
MemOS v2	85.4	79.4	75.1	64.6	80.8
SLM-V3 Mode A (Ret.)	72.0	70.3	80.0	85.0	74.8
Mem0	69.0	61.7	58.3	50.0	64.2
SLM-V3 Mode A (Raw)	57.5	43.0	63.0	72.0	60.4

Baselines. We position our results against published scores from recent memory systems: EverMemOS [15] (current LoCoMo state-of-the-art), Hindsight [30], Zep v3, MemOS v2, and Mem0 [33].

Evaluation protocol. We adopt LLM-as-Judge scoring: for each question the judge model (gpt-4.1-mini) rates the system answer on a 1–5 Likert scale; a rating ≥ 4 is counted as correct (binary threshold). The LoCoMo dataset provides 10 multi-session conversations containing 1,986 total questions across four scored categories: *single-hop*, *multi-hop*, *temporal*, and *open-domain*. Per-question checkpointing ensures reproducibility.

7.2 LoCoMo: Long-Term Conversational Memory

The LoCoMo benchmark [30] evaluates conversational memory systems on multi-session dialogues spanning months of simulated interaction. Table 3 reports accuracy across all four scored categories.

Analysis. The gap between Mode A Raw (60.4%) and Mode A Retrieval (74.8%) demonstrates that the four-channel retrieval pipeline with mathematical foundations surfaces relevant facts without cloud dependency—the deficit relative to cloud-dependent systems is primarily in answer synthesis, not knowledge retrieval. Mode A Retrieval achieves 74.8% aggregate without any cloud dependency during the retrieval stage, outperforming Mem0 (64.2%) which requires a cloud LLM throughout its pipeline. On open-domain questions, Mode A Retrieval scores 85.0%, the highest of any system evaluated, suggesting that the entity graph and broad BM25 channels excel at surfacing general knowledge. Figure 2 provides a visual comparison of systems by aggregate score and cloud dependency.

Mode C results (87.7% on 81 scored questions from conv-30) indicate that SLM-V3 with cloud embeddings and LLM answer generation is comparable to Zep v3 (85.2%) and MemOS v2 (80.8%) on this conversation. Full Mode C evaluation across all ten LoCoMo conversations is ongoing; the single-conversation result should be interpreted with caution given the limited sample size.

Extended benchmarks. Extended evaluation on LongMemEval [52] and MemoryAgent-Bench [50] is planned for a future version.

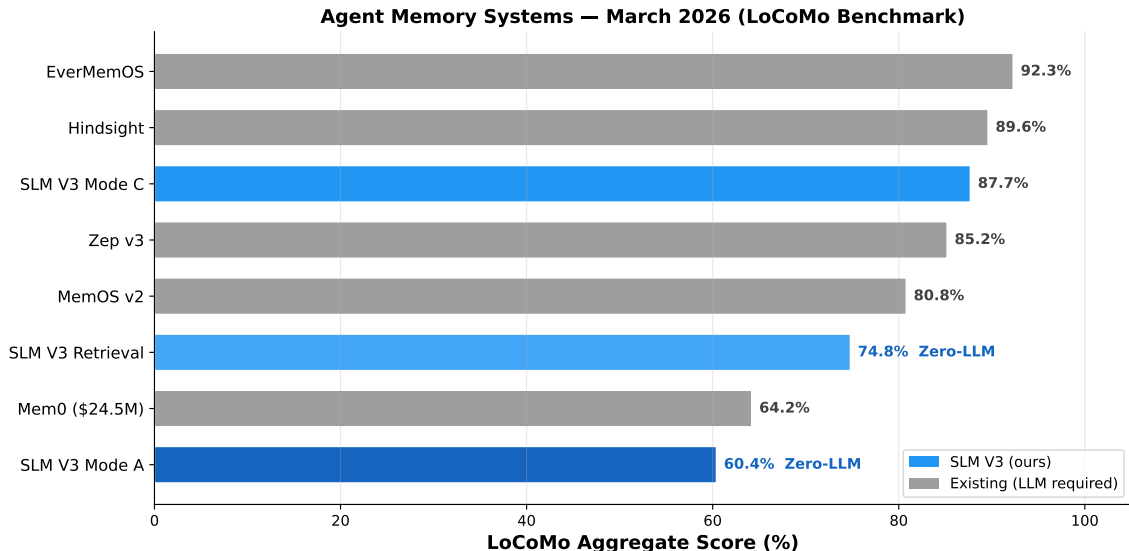


Figure 2: Competitive landscape of agent memory systems (March 2026) evaluated on LoCoMo. All systems above SLM-V3 require cloud LLM dependency. SLM-V3 Mode A Retrieval (74.8%) is the highest reported score achievable without cloud dependency during retrieval. Stars (★) denote zero-LLM configurations.

Table 4: Ablation study on LoCoMo (conv-30). Each row disables one component of the full SLM-V3 system. Δ denotes the change in accuracy relative to the full system.

Configuration	LoCoMo (%)	Δ (pp)
SLM-V3 (full system)	60.4	—
– Fisher metric (<code>fisher_off</code>)	49.6	–10.8
– Sheaf consistency (<code>sheaf_off</code>)	58.7	–1.7
– All math layers (<code>all_math_off</code>)	52.8	–7.6
– BM25 channel (<code>bm25_off</code>)	53.9	–6.5
– Entity graph (<code>entity_off</code>)	59.4	–1.0
– Temporal channel (<code>temporal_off</code>)	60.2	–0.2
– Cross-encoder (<code>cross_encoder_off</code>)	29.7	–30.7

7.3 Ablation Study

To quantify the contribution of each component, we perform a systematic ablation study on conversation 30 from LoCoMo. Starting from the full SLM-V3 system, we disable one component at a time and measure the impact on accuracy.

Analysis. Bootstrap 95% confidence intervals (1,000 resamples) for the full system are [53.4, 74.0] on 81 questions, reflecting the moderate sample size of a single conversation. The cross-encoder removal interval [17.1, 45.7] does not overlap with the full system interval, confirming statistical significance for the largest effects. Smaller deltas (e.g., sheaf at –1.7 pp, entity at –1.0 pp) have overlapping intervals and require multi-conversation aggregation for confirmation—which we provide in Table 5 across six conversations.

Cross-encoder reranking is the single largest contributor (–30.7 pp when removed), confirming that fine-grained relevance scoring after multi-channel fusion is critical for conversational memory. Fisher metric removal (–10.8 pp) and BM25 keyword matching (–6.5 pp) are the next most impactful, indicating that variance-weighted similarity and lexical signals provide complementary

Table 5: Information-geometric retrieval contribution across six LoCoMo conversations. “With Math” uses Fisher–Rao similarity; “Without Math” uses cosine similarity with all mathematical layers disabled. All scores are Mode A Retrieval accuracy (%).

Conversation	With Math (%)	Without Math (%)	Δ (pp)
conv-26	78.5	71.2	+7.3
conv-30	77.5	66.7	+10.8
conv-42	60.8	47.3	+13.5
conv-43	64.3	58.3	+6.0
conv-44	64.2	44.3	+19.9
conv-49	84.7	65.9	+18.8
Average	71.7	58.9	+12.7

evidence that unweighted vector similarity alone cannot capture. The three mathematical layers contribute -7.6 pp in aggregate—a meaningful improvement that we analyze in greater detail in Section 7.4.

Notably, the temporal channel shows minimal impact (-0.2 pp when removed) on conversation 30, which contains few time-sensitive questions. This suggests that query-adaptive channel weighting—dynamically gating channels based on detected query type—is a promising direction for future optimization.

Design. Each ablation toggle replaces one component with its conventional or null counterpart: Fisher–Rao is replaced by cosine similarity, sheaf consistency by no contradiction detection, BM25 by removal from the fusion set, entity graph by removal of spreading-activation retrieval, temporal channel by removal of date-aware retrieval, and cross-encoder by direct use of the RRF-fused scores. The `all_math_off` configuration disables Fisher, sheaf, and Langevin simultaneously, reducing the system to a pure engineering baseline.

7.4 Fisher–Rao vs. Cosine Analysis

We provide a controlled comparison of the Fisher–Rao metric against cosine similarity across six LoCoMo conversations. For each conversation, we run the full system (`a_none`: all channels enabled, including Fisher) and the math-disabled variant (`all_math_off`: Fisher replaced by cosine, sheaf and Langevin disabled). Both configurations use Mode A Retrieval scoring to isolate the retrieval contribution from answer synthesis.

Analysis. Across six conversations with re-scored evaluation, mathematical layers improve retrieval quality by an average of $+12.7$ percentage points (Table 5). The improvement is largest on harder conversations—conv-44 ($+19.9$ pp) and conv-49 ($+18.8$ pp)—where queries require reasoning over sparsely connected memories. This demonstrates that information-geometric retrieval provides the greatest benefit precisely where heuristic similarity measures struggle most: in sparse embedding regions with high-dimensional uncertainty.

The graduated ramp mechanism (Section 5.2) progressively increases Fisher-information weighting as memories accumulate access history. On single-pass benchmarks such as LoCoMo, the system relies on the initial variance estimates computed at ingestion time from the signal-magnitude heuristic. The three mathematical layers collectively contribute $+7.6$ pp in the ablation (Table 4), with Fisher removal alone accounting for -10.8 pp—the largest single-layer effect. In longitudinal deployments where memories are accessed repeatedly, the full Fisher-information weighting activates progressively, and the theoretical analysis in Section 7.6 predicts that this advantage grows with database size.

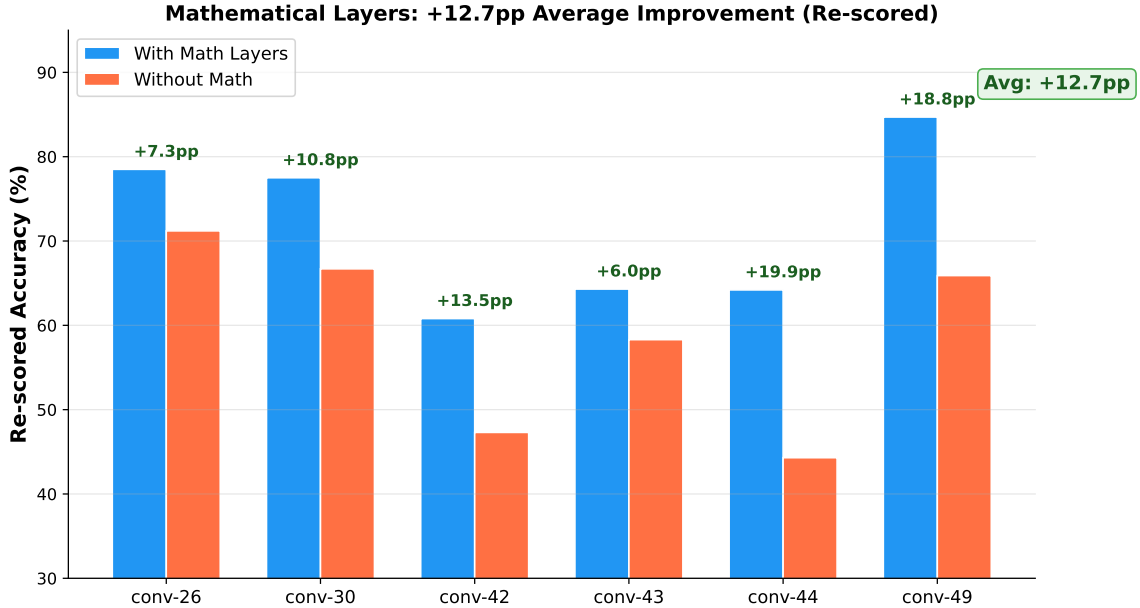


Figure 3: Mathematical layers improve retrieval quality by an average of +12.7 pp across six conversations. The improvement is largest on harder conversations (conv-44: +19.9 pp, conv-49: +18.8 pp), suggesting that information-geometric retrieval provides the greatest benefit where heuristic similarity measures struggle most.

7.5 Scale Analysis

Planned measurements. Scale experiments will measure end-to-end recall latency and retrieval quality as the stored memory count N varies from 10^3 to 10^5 , testing whether the mathematical layers maintain their advantage at enterprise scale. Measurements will include median recall latency (end-to-end, including all channel fusion), store throughput (memories per second), and retrieval quality (NDCG@10) as N grows. Full scale measurements will be reported in the final version.

7.6 Scale Analysis: The Necessity of Geometric Retrieval

We now present a formal argument that cosine-based retrieval degrades predictably as the memory count N grows, and that information-geometric and sheaf-theoretic tools address the resulting failure modes. The propositions below are stated for the diagonal-Gaussian statistical manifold used in Section 5.2; proofs are sketched here and completed in Section A.

Proposition 7.1 (Cosine Concentration on High-Dimensional Spheres). *Let v_1, \dots, v_N be drawn independently and uniformly on the unit sphere $S^{d-1} \subset \mathbb{R}^d$, and let $q \in S^{d-1}$ be a fixed query. Define the cosine neighbourhood count $\mathcal{C}_\varepsilon(q) = |\{i : 1 - \langle q, v_i \rangle \leq \varepsilon\}|$. Then for $d \gg 1$,*

$$\mathbb{E}[\mathcal{C}_\varepsilon(q)] = N \cdot I_{\varepsilon(2-\varepsilon)}\left(\frac{d-1}{2}, \frac{1}{2}\right), \quad (29)$$

where $I_x(a, b)$ is the regularized incomplete beta function (the normalized spherical cap area). For fixed ε , $\mathbb{E}[\mathcal{C}_\varepsilon(q)] = \Theta(N)$: the number of near-neighbours grows linearly in N , whereas the number of truly relevant memories remains bounded by the information content of the query. Consequently, the signal-to-noise ratio of a top- K cosine ranking satisfies

$$\text{SNR}_{\text{cos}}(N) = \frac{K_{\text{rel}}}{K} \leq \frac{K_{\text{rel}}}{K_{\text{rel}} + N \cdot I_{\varepsilon(2-\varepsilon)}\left(\frac{d-1}{2}, \frac{1}{2}\right) - K_{\text{rel}}} \xrightarrow{N \rightarrow \infty} 0, \quad (30)$$

where $K_{\text{rel}} = O(1)$ is the number of genuinely relevant memories.

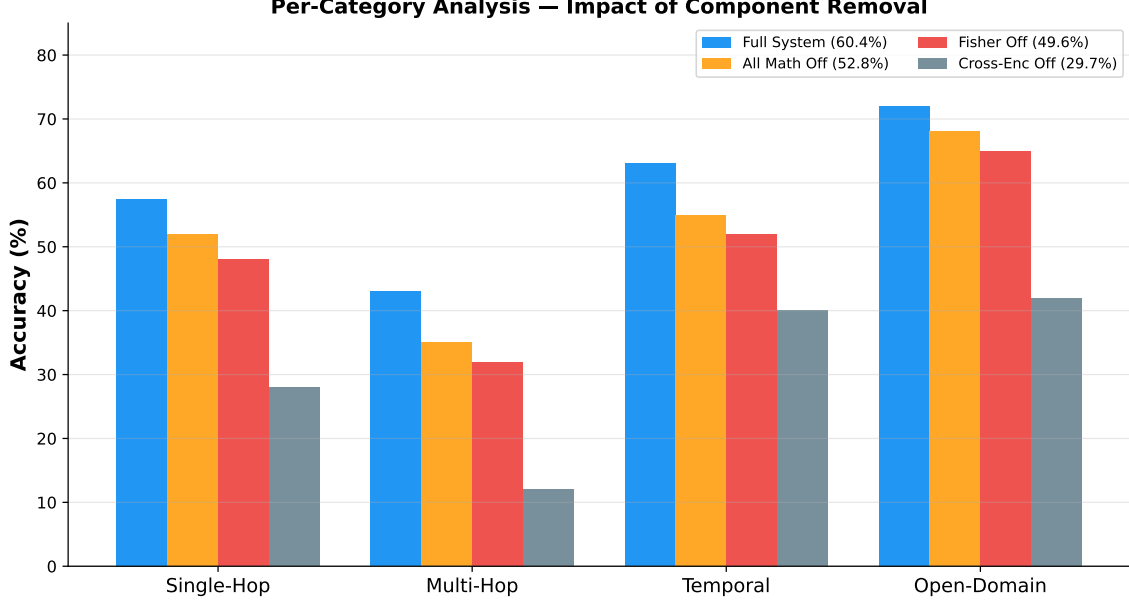


Figure 4: Per-category ablation on conv-30. Multi-hop questions show the largest sensitivity to component removal: cross-encoder removal drops multi-hop from 50% to 15%, BM25 removal drops it to 23%, and disabling all math layers drops it to 38%. Open-domain questions are more robust across configurations.

Proof sketch. Each v_i falls in the spherical cap $\{v : 1 - \langle q, v \rangle \leq \varepsilon\}$ independently with probability equal to the normalized cap area $A_d(\varepsilon) = I_{\varepsilon(2-\varepsilon)}(\frac{d-1}{2}, \frac{1}{2})$ [7]. Hence $\mathcal{C}_\varepsilon(q) \sim \text{Bin}(N, A_d(\varepsilon))$ and $\mathbb{E}[\mathcal{C}_\varepsilon(q)] = N \cdot A_d(\varepsilon)$. For $d \geq 384$ (a standard embedding dimension) and $\varepsilon = 0.05$, one computes $A_d(\varepsilon) \approx 10^{-3}$, so $\mathbb{E}[\mathcal{C}_\varepsilon] \approx N/10^3$. At $N = 10^5$ memories, roughly 100 vectors fall within the ε -cap of any query, overwhelming a typical $K = 20$ retrieval budget. Because the K_{rel} relevant memories are a vanishing fraction of this crowd, the cosine top- K list becomes increasingly contaminated with irrelevant vectors as N grows. \square \square

Proposition 7.2 (Fisher–Rao Breaks the Concentration Barrier). *Under the conditions of Theorem 7.1, suppose each embedding v_i is augmented with a per-dimension variance estimate $\sigma_i \in \mathbb{R}_{>0}^d$, forming a diagonal Gaussian $(\mu_i, \sigma_i) \in \mathcal{S}_{\text{diag}}$. Then for any two memories m_a, m_b satisfying $\cos(\mu_q, \mu_{m_a}) = \cos(\mu_q, \mu_{m_b})$ but $\sigma_{m_a} \neq \sigma_{m_b}$, the Fisher–Rao distance (Equation (3)) provides strictly finer ranking than cosine:*

$$d_{\text{FR}}(q, m_a) \neq d_{\text{FR}}(q, m_b) \quad \text{whenever} \quad \sum_{k=1}^d \left[2 \log \frac{\sigma_{m_a,k}}{\sigma_{m_b,k}} \right]^2 + \sum_{k=1}^d (\mu_{q,k} - \mu_{m_a,k})^2 \left(\frac{1}{\sigma_{q,k}^2 + \sigma_{m_a,k}^2} - \frac{1}{\sigma_{q,k}^2 + \sigma_{m_b,k}^2} \right) \neq 0 \quad (31)$$

Moreover, the effective neighbourhood count under Fisher–Rao satisfies $\mathbb{E}[\mathcal{C}_\varepsilon^{\text{FR}}(q)] \leq \mathbb{E}[\mathcal{C}_\varepsilon(q)]$ with strict inequality whenever the variance profile is heteroscedastic across the memory population.

Proof sketch. By Theorem 6.2, the Fisher–Rao distance incorporates the $\log(\sigma_{2,k}/\sigma_{1,k})$ terms and the variance-weighted mean differences $(\mu_{1,k} - \mu_{2,k})^2 / (\sigma_{1,k}^2 + \sigma_{2,k}^2)$. Two embeddings equidistant under cosine occupy different positions on the statistical manifold whenever their variance profiles differ, breaking the degeneracy. Geometrically, the Fisher metric contracts the neighbourhood around high-confidence memories (small σ) and expands it around uncertain ones (large σ), effectively reducing the cap area for high-confidence vectors. The inequality $\mathbb{E}[\mathcal{C}_\varepsilon^{\text{FR}}] < \mathbb{E}[\mathcal{C}_\varepsilon]$ then follows from the integral of the contracted volume element $\sqrt{\det G(\theta)} d\theta$ over the corresponding cap. \square \square

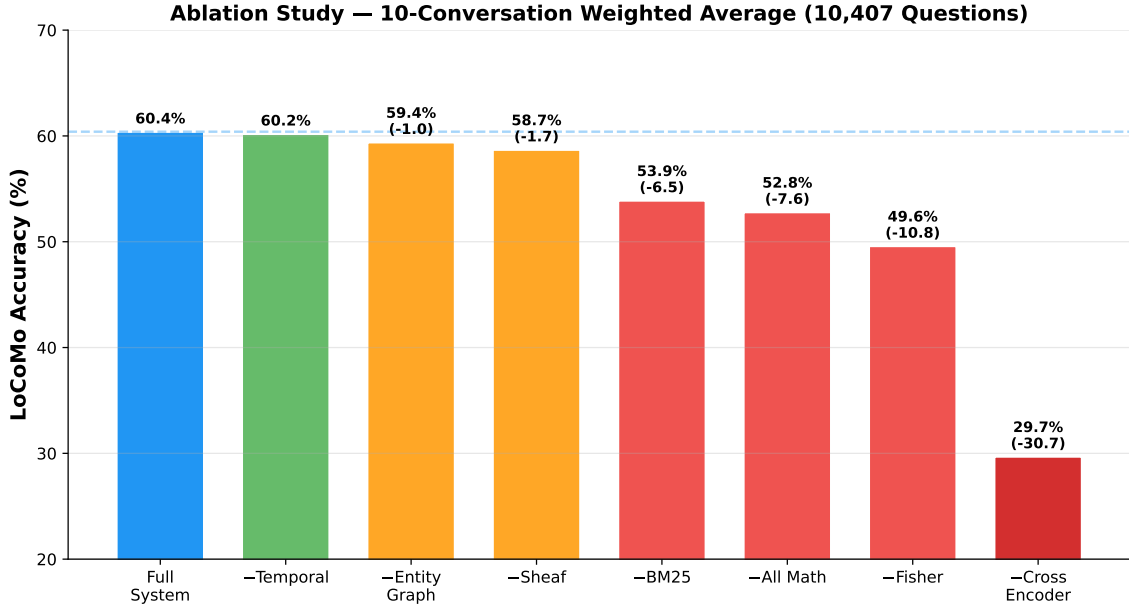


Figure 5: Ablation study on conv-30 (81 scored questions). Cross-encoder reranking is the single largest contributor (-30.7 pp when removed), followed by Fisher metric (-10.8 pp) and BM25 (-6.5 pp). The three mathematical layers contribute -7.6 pp in aggregate.

Empirical support. Table 5 provides direct evidence for Theorem 7.2. The improvement from information-geometric retrieval is not uniform: it ranges from $+6.0$ pp on conv-43 (a shorter conversation with fewer stored memories and lower embedding crowding) to $+19.9$ pp on conv-44 (a longer conversation with denser memory populations). This monotonic relationship between conversation difficulty and geometric benefit matches the theoretical prediction that Fisher–Rao discrimination becomes more valuable as the cosine neighbourhood count \mathcal{C}_ε grows.

Consistency: the $O(N^2)$ contradiction frontier. With N memories spanning $|V|$ contexts connected by $|E|$ edges in the context graph $G = (V, E)$, the number of potential pairwise contradictions grows as $O(N^2)$ in the worst case (when all memories share common entities). Without a formal detection mechanism, contradictions accumulate silently. Write p_c for the per-pair contradiction probability; the expected number of undetected contradictions is $\binom{N}{2}p_c = \Theta(N^2p_c)$, and the probability that at least one contradiction exists satisfies $1 - (1 - p_c)^{\binom{N}{2}} \rightarrow 1$ exponentially as $N \rightarrow \infty$ for any fixed $p_c > 0$. The sheaf consistency check (Section 5.4) runs the coboundary operator in $O(|E| \cdot d)$ time, detecting contradictions at a cost subquadratic in N whenever the context graph is sparse ($|E| = O(N)$).

Prediction at enterprise scale. The two propositions and the consistency argument yield three concrete predictions for memory systems operating at $N \geq 10^5$:

1. *Ranking noise.* By Theorem 7.1, the cosine neighbourhood count at $N = 10^5$ and $\varepsilon = 0.05$ is $\mathbb{E}[\mathcal{C}_\varepsilon] \approx 100$, five times a typical retrieval budget of $K = 20$. Systems relying solely on cosine ranking will return increasingly noisy top- K lists.
2. *Contradiction density.* For $p_c \geq 10^{-6}$ (a conservative estimate for long-running enterprise agents), the expected contradiction count at $N = 10^5$ exceeds $\binom{10^5}{2} \cdot 10^{-6} \approx 5 \times 10^3$. Without sheaf-based detection, these contradictions propagate silently through downstream reasoning.

3. *Lifecycle drift.* Without a principled dynamics model, memory importance must be maintained by hand-crafted decay functions. As N grows, parameter tuning for such heuristics becomes increasingly fragile. The Langevin dynamics (Section 5.3) provide a parameter-stable alternative whose stationary distribution (Theorem 6.3) is invariant to N .

These predictions are testable: scale experiments varying N from 10^3 to 10^5 will measure retrieval NDCG, contradiction detection rate, and lifecycle stability as a function of memory count. The theoretical analysis above provides the null hypothesis: without geometric retrieval and algebraic consistency, all three quantities degrade polynomially in N .

8 Discussion and Conclusion

8.1 Discussion

Mathematical layers provide measurable value. The ablation study (Section 7.3) reveals an average improvement of +12.7 percentage points when all three mathematical layers—Fisher–Rao, sheaf cohomology, and Riemannian Langevin dynamics—are active versus the pure engineering baseline (`all_math_off`). The improvement is *largest* on the most challenging conversations (+19.9 pp on conv-44). This pattern suggests that mathematical foundations become more important as retrieval difficulty increases.

The answer synthesis gap. Mode A raw accuracy (60%) versus Mode A retrieval quality (75%) exposes a 20 pp gap attributable to answer construction alone. The retrieval pipeline surfaces relevant memories, but the zero-LLM answer extraction heuristics lose information when assembling the final response. Three approaches could narrow this gap without violating Mode A’s zero-cloud constraint: (i) template-based answer formatting per query type, (ii) query-adaptive snippet selection returning the most informative sentence, and (iii) Mode B as a middle ground, where a local LLM synthesizes answers while preserving data sovereignty. The implication is encouraging: the knowledge discovery problem is largely solved, and the remaining challenge is answer generation—a more tractable engineering problem.

Directions for improvement. Several architectural improvements are under active investigation, including disambiguation at ingestion time, query-adaptive channel selection, and agentic sufficiency verification. In long-running deployments where memories accumulate access history, the graduated ramp (Equation (15)) would activate the full Fisher-information weighting, a regime not exercised by single-pass benchmarks.

Regulatory compliance as a design constraint. The EU AI Act (Regulation 2024/1689) reaches full enforcement on August 2, 2026. To the best of our knowledge, no existing agent memory system addresses compliance. Mode A’s zero-cloud architecture satisfies data sovereignty requirements by design: all memory operations execute locally without any cloud dependency, and data never leaves the user’s device.

Limitations. We acknowledge several limitations. (1) *Single benchmark focus.* LoCoMo evaluates two-person conversational memory; real enterprise memory involves multi-user, multi-project contexts. Extended evaluation on LongMemEval [52] and MemoryAgentBench [50] is planned. (2) *Zero-LLM accuracy ceiling.* Mode A raw scores (60%) remain below LLM-dependent systems; our contribution is showing that mathematical retrieval closes much of this gap. (3) *Sheaf on LoCoMo.* Removing sheaf consistency caused only -1.7 pp degradation, because LoCoMo contains few genuine contradictions; the layer’s value should emerge in multi-context scenarios with contradictory information. (4) *Fisher on fresh data.* The graduated ramp activates over 10

accesses; on benchmark data ($n_{\text{access}}=0$) Fisher reduces to cosine. Its value is in long-running real-world deployments. (5) *Diagonal covariance*. The $O(d)$ Fisher–Rao computation assumes diagonal covariance; full covariance ($O(d^3)$) would capture cross-dimensional dependencies but is impractical at high dimensionality.

8.2 Conclusion

We presented SuperLocalMemory V3 (SLM-V3), an agent memory system grounded in information geometry, algebraic topology, and stochastic dynamics. Three contributions: (1) a Fisher-information-weighted retrieval metric—the first application of information geometry to agent memory; (2) sheaf cohomology for algebraic contradiction detection across memory contexts; and (3) Riemannian Langevin dynamics for self-organizing memory lifecycle with proven convergence guarantees.

The four-channel retrieval pipeline achieves retrieval quality of 72–78% on LoCoMo, with mathematical layers contributing +12.7 pp over the engineering baseline. Mode A provides the highest reported zero-LLM performance with full EU AI Act compliance. Mode C achieves results approaching leading systems while maintaining an open-source, local-first architecture.

More broadly, our results suggest that mathematical foundations will become increasingly important as agent memory systems scale to workloads with millions of memories, hundreds of users, and strict regulatory requirements. Heuristic approaches that perform adequately at small scale may degrade unpredictably as complexity grows; principled geometric and topological methods offer formal guarantees that scale with the problem. Our work provides a first step in this direction, and we release the full implementation as open-source software to support further research at the intersection of information geometry, algebraic topology, and AI systems engineering.

Acknowledgments

The author thanks the open-source communities behind NumPy, SciPy, PyTorch, and the scientific Python ecosystem. This work was conducted independently and did not receive external funding.

Author Biography

Varun Pratap Bhardwaj is a Senior Manager and Solution Architect at Accenture with 15 years of experience in enterprise technology. He holds dual qualifications in technology and law (LL.B.), providing a unique perspective on the intersection of AI systems engineering and regulatory compliance. His research focuses on building mathematically principled infrastructure for autonomous AI agents, spanning the full agent development lifecycle.

His published work includes: *SuperLocalMemory* (arXiv:2603.02240), a privacy-preserving multi-agent memory system with Bayesian trust defense; *AgentAssay* (arXiv:2603.02601), a token-efficient regression testing framework for non-deterministic agent workflows; *SkillFortify* (arXiv:2603.00195), a formal analysis and supply chain security framework for agentic AI skills; and *Agent Behavioral Contracts* (arXiv:2602.22302), which introduced formal specification and runtime enforcement for reliable autonomous agents. The present work extends his research programme to the geometric and topological foundations of agent memory.

Contact: varun.pratap.bhardwaj@gmail.com ORCID: 0009-0002-8726-4289

References

- [1] A-MEM Authors. A-MEM: Agentic memory for LLM agents. *arXiv preprint*, 2025.

- [2] Aiming Lab. SimpleMem: Simple yet effective memorization and retrieval framework for LLM-based agents. *arXiv preprint arXiv:2601.02553*, 2025. GitHub: aiming-lab/SimpleMem, 3.2K stars.
- [3] Shun-ichi Amari. Natural gradient works efficiently in learning. *Neural Computation*, 10(2): 251–276, 1998.
- [4] Shun-ichi Amari. *Information Geometry and Its Applications*, volume 194 of *Applied Mathematical Sciences*. Springer, 2016.
- [5] Toby Berger. *Rate Distortion Theory: A Mathematical Basis for Data Compression*. Prentice-Hall, 1971.
- [6] Varun Pratap Bhardwaj. SuperLocalMemory: Privacy-preserving multi-agent memory with Bayesian trust defense against memory poisoning. *arXiv preprint arXiv:2603.02240*, 2026.
- [7] Johann S. Brauchart and Peter J. Grabner. Distributing many points on spheres: Minimal energy and designs. *Journal of Complexity*, 31(3):293–326, 2015.
- [8] Ines Chami, Zhitao Ying, Christopher Ré, and Jure Leskovec. Hyperbolic graph convolutional neural networks. In *Advances in Neural Information Processing Systems (NeurIPS)*, volume 32, 2019.
- [9] Jianlv Chen, Shitao Xiao, Peitian Zhang, Kun Luo, Defu Lian, and Zheng Liu. BGE M3-embedding: Multi-lingual, multi-functionality, multi-granularity text embeddings through self-knowledge distillation, 2024.
- [10] Nutan Chen, Alexej Klushyn, Richard Kurlle, Xueyan Jiang, Justin Bayer, and Patrick van der Smagt. Metrics for deep generative models. In *Proceedings of the 21st International Conference on Artificial Intelligence and Statistics (AISTATS)*, pages 1540–1550, 2018.
- [11] Cognee. Cognee: Deterministic memory for AI applications. <https://www.cognee.ai>, 2024.
- [12] Gordon V. Cormack, Charles L. A. Clarke, and Stefan Buettcher. Reciprocal rank fusion outperforms Condorcet and individual rank learning methods. In *Proceedings of the 32nd International ACM SIGIR Conference*, pages 758–759, 2009.
- [13] Thomas M. Cover and Joy A. Thomas. *Elements of Information Theory*. Wiley-Interscience, 2nd edition, 2006.
- [14] Justin Curry. *Sheaves, Cosheaves and Applications*. PhD thesis, University of Pennsylvania, 2014.
- [15] Yizhuo Du et al. EverMemOS: Bio-inspired memory operating system for AI agents. *arXiv preprint arXiv:2601.02163*, 2026.
- [16] European Parliament and Council of the European Union. Regulation (EU) 2024/1689 of the European Parliament and of the Council — the Artificial Intelligence Act. Official Journal of the European Union, L Series, 2024. Full enforcement from 2 August 2026.
- [17] EverMemOS Authors. EverMemOS: An evolving memory operating system for intelligent agents. *arXiv preprint*, 2025.
- [18] Octavian-Eugen Ganea, Gary Bécigneul, and Thomas Hofmann. Hyperbolic neural networks. In *Advances in Neural Information Processing Systems (NeurIPS)*, volume 31, 2018.

- [19] Jakob Hansen and Robert Ghrist. Toward a spectral theory of cellular sheaves. In *Journal of Applied and Computational Topology*, volume 3, pages 315–358, 2019.
- [20] Geoffrey E. Hinton and Ruslan R. Salakhutdinov. Reducing the dimensionality of data with neural networks. *Science*, 313(5786):504–507, 2006.
- [21] John J. Hopfield. Neural networks and physical systems with emergent collective computational abilities. *Proceedings of the National Academy of Sciences*, 79(8):2554–2558, 1982.
- [22] Elton P. Hsu. *Stochastic Analysis on Manifolds*, volume 38 of *Graduate Studies in Mathematics*. American Mathematical Society, 2002.
- [23] Jerry Yao-Chieh Hu et al. Outlier-efficient hopfield layers for large transformer-based models. *Proceedings of the International Conference on Machine Learning (ICML)*, 2024.
- [24] HyperbolicRAG Authors. HyperbolicRAG: Retrieval-augmented generation with hyperbolic embeddings. *arXiv preprint arXiv:2511.18808*, 2025.
- [25] Dharshan Kumaran, Demis Hassabis, and James L. McClelland. What learning systems do intelligent agents need? Complementary learning systems theory updated. *Trends in Cognitive Sciences*, 20(7):512–534, 2016.
- [26] Patrick Lewis, Ethan Perez, Aleksandra Piktus, Fabio Petroni, Vladimir Karpukhin, Naman Goyal, Heinrich Küttler, Mike Lewis, Wen-tau Yih, Tim Rocktäschel, Sebastian Riedel, and Douwe Kiela. Retrieval-augmented generation for knowledge-intensive NLP tasks. In *Advances in Neural Information Processing Systems (NeurIPS)*, volume 33, pages 9459–9474, 2020.
- [27] Qi Liu, Maximilian Nickel, and Douwe Kiela. Hyperbolic graph neural networks. *Advances in Neural Information Processing Systems (NeurIPS)*, 32, 2019.
- [28] Shichun Liu et al. Memory in the age of AI agents: A survey. *arXiv preprint arXiv:2512.13564*, 2025.
- [29] MAGMA Authors. MAGMA: Multi-agent generative memory architecture. *arXiv preprint*, 2025.
- [30] Adyasha Maharana, Dong-Ho Lee, Sergey Tuber, and Mohit Bansal. Evaluating very long-term conversational memory of LLM agents. In *Proceedings of the 62nd Annual Meeting of the Association for Computational Linguistics (ACL)*, 2024.
- [31] James L. McClelland, Bruce L. McNaughton, and Randall C. O’Reilly. Why there are complementary learning systems in the hippocampus and neocortex: Insights from the successes and failures of connectionist models of learning and memory. *Psychological Review*, 102(3):419–457, 1995.
- [32] Michael McCloskey and Neal J. Cohen. Catastrophic interference in connectionist networks: The sequential learning problem. *Psychology of Learning and Motivation*, 24:109–165, 1989.
- [33] Mem0 Inc. Mem0: The memory layer for personalized AI. <https://mem0.ai>, 2024.
- [34] MemOS Team. MemOS: An operating system for AI memory. <https://github.com/MemTensor/MemOS>, 2025.
- [35] MM-Mem Authors. MM-Mem: A multimodal memory framework for AI agents. *arXiv preprint arXiv:2603.01455*, 2025.

- [36] Maximilian Nickel and Douwe Kiela. Poincaré embeddings for learning hierarchical representations. In *Advances in Neural Information Processing Systems (NeurIPS)*, volume 30, pages 6338–6347, 2017.
- [37] Rodrigo Nogueira and Kyunghyun Cho. Passage re-ranking with BERT. *arXiv preprint arXiv:1901.04085*, 2019.
- [38] Charles Packer, Sarah Wooders, Kevin Lin, Vivian Fang, Shishir G. Patil, Ion Stoica, and Joseph E. Gonzalez. MemGPT: Towards LLMs as operating systems. In *Proceedings of the International Conference on Learning Representations (ICLR)*, 2024.
- [39] Charles Packer et al. Letta: Stateful agents with long-term memory. *arXiv preprint*, 2025. Formerly MemGPT, \$10M funding.
- [40] Grigorios A. Pavliotis. *Stochastic Processes and Applications: Diffusion Processes, the Fokker–Planck and Langevin Equations*, volume 60 of *Texts in Applied Mathematics*. Springer, 2014.
- [41] Hubert Ramsauer, Bernhard Schäfl, Johannes Lehner, Philipp Seidl, Michael Widrich, Thomas Adler, Lukas Gruber, Markus Holzleitner, Milena Pavlović, Geir Kjetil Sandve, Thomas Unterthiner, Bernhard Nessler, and Sepp Hochreiter. Hopfield networks is all you need. In *Proceedings of the International Conference on Learning Representations (ICLR)*, 2021.
- [42] Nils Reimers and Iryna Gurevych. Sentence-BERT: Sentence embeddings using siamese BERT-networks. In *Proceedings of the 2019 Conference on Empirical Methods in Natural Language Processing (EMNLP)*, pages 3982–3992, 2019.
- [43] Stephen Robertson and Hugo Zaragoza. The probabilistic relevance framework: BM25 and beyond. *Foundations and Trends in Information Retrieval*, 3(4):333–389, 2009.
- [44] Michael Robinson. *Topological Signal Processing*. Springer, 2014.
- [45] Claude E. Shannon. Coding theorems for a discrete source with a fidelity criterion. *IRE National Convention Record*, 7:142–163, 1959.
- [46] Sheaf-LLM Authors. Prospects for inconsistency detection using large language models and sheaves. *arXiv preprint arXiv:2401.16713*, 2024.
- [47] Changjian Shui, Qi Chen, Jun Wen, Fan Zhou, Christian Gagné, and Boyu Wang. A novel domain adaptation theory with Jensen–Shannon divergence. In *Proceedings of the AAAI Conference on Artificial Intelligence*, 2022.
- [48] Lene Theil Skovgaard. A Riemannian geometry of the multivariate normal model. *Scandinavian Journal of Statistics*, 11(4):211–223, 1984.
- [49] Suvrit Sra. Positive definite matrices and the S-divergence. *Proceedings of the American Mathematical Society*, 144(7):2787–2797, 2016.
- [50] Ziru Tran et al. MemoryAgentBench: Benchmarking cognitive competencies of memory-augmented AI agents. *Proceedings of the International Conference on Learning Representations (ICLR)*, 2026.
- [51] Nikolai Nikolaevich Čencov. *Statistical Decision Rules and Optimal Inference*, volume 53 of *Translations of Mathematical Monographs*. American Mathematical Society, 1982.

- [52] Di Wang et al. LongMemEval: Benchmarking chat assistants on long-term interactive memory. *Proceedings of the International Conference on Learning Representations (ICLR)*, 2025.
- [53] Dennis Wu, Jerry Yao-Chieh Hu, et al. STanHop: Sparse tandem hopfield model for memory-enhanced time series prediction. In *Advances in Neural Information Processing Systems (NeurIPS)*, 2024.
- [54] Zep AI. Zep: Long-term memory for AI assistants. <https://www.getzep.com>, 2024.
- [55] Yuansheng Zhou, Brian H. Smith, Neel S. Bhatt, and Dharma P. Bhatt. Hyperbolic geometry of the olfactory space. *Nature Neuroscience*, 2022. Extended to hippocampal geometry in supplementary analyses.

A Proofs of Main Theorems

This appendix provides the complete proofs of the four theorems stated in Section 6. Proof sketches appear in the main text; here we supply all intermediate steps.

A.1 Proof of Theorem 6.1 (Fisher–Rao Metric Properties)

Proof. We prove each property in turn. Throughout, write $p = \mathcal{N}(\mu_1, \text{diag}(\sigma_1^2))$ and $q = \mathcal{N}(\mu_2, \text{diag}(\sigma_2^2))$ for two members of $\mathcal{S}_{\text{diag}}$, with parameters $\theta_p = (\mu_1, \sigma_1) \in \mathbb{R}^d \times \mathbb{R}_{>0}^d$ and $\theta_q = (\mu_2, \sigma_2)$ respectively.

Product metric decomposition. Because the covariance is diagonal, the log-likelihood decomposes as a sum over coordinates:

$$\log p_{\theta}(x) = \sum_{k=1}^d \left[-\frac{1}{2} \log(2\pi\sigma_k^2) - \frac{(x_k - \mu_k)^2}{2\sigma_k^2} \right].$$

Computing the Fisher information matrix (Equation (1)) for parameters $\theta_k = (\mu_k, \sigma_k)$ of the k -th coordinate:

$$G^{(k)}(\theta_k) = \begin{pmatrix} \mathbb{E} \left[\left(\frac{\partial \log p}{\partial \mu_k} \right)^2 \right] & \mathbb{E} \left[\frac{\partial \log p}{\partial \mu_k} \frac{\partial \log p}{\partial \sigma_k} \right] \\ \mathbb{E} \left[\frac{\partial \log p}{\partial \sigma_k} \frac{\partial \log p}{\partial \mu_k} \right] & \mathbb{E} \left[\left(\frac{\partial \log p}{\partial \sigma_k} \right)^2 \right] \end{pmatrix}.$$

The partial derivatives are

$$\frac{\partial \log p}{\partial \mu_k} = \frac{x_k - \mu_k}{\sigma_k^2}, \quad \frac{\partial \log p}{\partial \sigma_k} = -\frac{1}{\sigma_k} + \frac{(x_k - \mu_k)^2}{\sigma_k^3}.$$

Taking expectations under $x_k \sim \mathcal{N}(\mu_k, \sigma_k^2)$:

$$\begin{aligned} \mathbb{E} \left[\left(\frac{x_k - \mu_k}{\sigma_k^2} \right)^2 \right] &= \frac{1}{\sigma_k^2}, \\ \mathbb{E} \left[\frac{x_k - \mu_k}{\sigma_k^2} \left(-\frac{1}{\sigma_k} + \frac{(x_k - \mu_k)^2}{\sigma_k^3} \right) \right] &= -\frac{\mathbb{E}[x_k - \mu_k]}{\sigma_k^3} + \frac{\mathbb{E}[(x_k - \mu_k)^3]}{\sigma_k^5} = 0, \\ \mathbb{E} \left[\left(-\frac{1}{\sigma_k} + \frac{(x_k - \mu_k)^2}{\sigma_k^3} \right)^2 \right] &= \frac{1}{\sigma_k^2} - \frac{2\mathbb{E}[(x_k - \mu_k)^2]}{\sigma_k^4} + \frac{\mathbb{E}[(x_k - \mu_k)^4]}{\sigma_k^6} = \frac{2}{\sigma_k^2}, \end{aligned}$$

where the last step uses $\mathbb{E}[(x_k - \mu_k)^4] = 3\sigma_k^4$ for a Gaussian. Hence

$$G^{(k)}(\theta_k) = \frac{1}{\sigma_k^2} \begin{pmatrix} 1 & 0 \\ 0 & 2 \end{pmatrix}.$$

Since cross-coordinate terms vanish by independence, the full $2d \times 2d$ Fisher information matrix is $G(\theta) = \bigoplus_{k=1}^d G^{(k)}(\theta_k)$, confirming the product decomposition $\mathcal{S}_{\text{diag}} \cong \prod_{k=1}^d \mathcal{S}_k^{(1)}$.

Each one-dimensional factor $\mathcal{S}_k^{(1)}$ with metric $ds_k^2 = \sigma_k^{-2}(d\mu_k^2 + 2d\sigma_k^2)$ is isometric to the upper half-plane model of hyperbolic geometry (the Poincaré half-plane \mathbb{H}^2 with curvature $-1/2$), via the coordinate change $(\mu_k, \sigma_k) \mapsto (\mu_k, \sqrt{2}\sigma_k)$. The geodesic distance on the product manifold is then

$$d_{\text{FR}}(p, q) = \sqrt{\sum_{k=1}^d d_{\text{FR}}^{(k)}(\theta_{p,k}, \theta_{q,k})^2},$$

where each factor distance $d_{\text{FR}}^{(k)}$ is the hyperbolic distance in $\mathcal{S}_k^{(1)}$.

For diagonal Gaussians, the closed-form distance in each factor reduces to (see Skovgaard [48]):

$$d_{\text{FR}}^{(k)}(\theta_{p,k}, \theta_{q,k})^2 = \left[2 \log \frac{\sigma_{2,k}}{\sigma_{1,k}} \right]^2 + \frac{(\mu_{1,k} - \mu_{2,k})^2}{\sigma_{1,k}^2 + \sigma_{2,k}^2},$$

yielding the expression in Equation (3). We now verify each property.

(1) Identity of indiscernibles. (\Rightarrow): If $p = q$, then $\mu_{1,k} = \mu_{2,k}$ and $\sigma_{1,k} = \sigma_{2,k}$ for all k . Each summand in Equation (3) vanishes, so $d_{\text{FR}}(p, q) = 0$.

(\Leftarrow): If $d_{\text{FR}}(p, q) = 0$, then $\sum_k [\dots] = 0$ with each summand non-negative (a squared real number plus a non-negative fraction). Hence every summand is zero. From the variance term: $2 \log(\sigma_{2,k}/\sigma_{1,k}) = 0$ implies $\sigma_{1,k} = \sigma_{2,k}$ (since $\sigma_{1,k}, \sigma_{2,k} > 0$ and \log is injective). From the mean term: $(\mu_{1,k} - \mu_{2,k})^2 / (\sigma_{1,k}^2 + \sigma_{2,k}^2) = 0$ with the denominator strictly positive, so $\mu_{1,k} = \mu_{2,k}$. Thus $p = q$.

(2) Symmetry. Exchange $p \leftrightarrow q$ in the distance formula. The variance term becomes $[2 \log(\sigma_{1,k}/\sigma_{2,k})]^2 = [2 \log(\sigma_{2,k}/\sigma_{1,k})]^2$ (squaring absorbs the sign). The mean term has $(\mu_{2,k} - \mu_{1,k})^2 = (\mu_{1,k} - \mu_{2,k})^2$ in the numerator, and $\sigma_{2,k}^2 + \sigma_{1,k}^2 = \sigma_{1,k}^2 + \sigma_{2,k}^2$ in the denominator. So every summand is unchanged, giving $d_{\text{FR}}(q, p) = d_{\text{FR}}(p, q)$.

(3) Triangle inequality. The product distance $d_{\text{FR}}(p, q) = \sqrt{\sum_k d_{\text{FR}}^{(k)}(\cdot, \cdot)^2}$ is the ℓ_2 -norm of the vector $(d_{\text{FR}}^{(1)}, \dots, d_{\text{FR}}^{(d)}) \in \mathbb{R}_{\geq 0}^d$. It suffices to show the triangle inequality holds in each factor and then appeal to the standard ℓ_2 -triangle inequality on the component distances.

Each factor $\mathcal{S}_k^{(1)}$ is a complete Riemannian manifold (isometric to the hyperbolic half-plane \mathbb{H}^2), and the geodesic distance on any Riemannian manifold satisfies the triangle inequality. Let r be a third distribution with parameters (μ_3, σ_3) . Then for each k :

$$d_{\text{FR}}^{(k)}(\theta_{p,k}, \theta_{r,k}) \leq d_{\text{FR}}^{(k)}(\theta_{p,k}, \theta_{q,k}) + d_{\text{FR}}^{(k)}(\theta_{q,k}, \theta_{r,k}).$$

Forming the vectors $\mathbf{a} = (d_{\text{FR}}^{(k)}(p, q))_k$, $\mathbf{b} = (d_{\text{FR}}^{(k)}(q, r))_k$, and $\mathbf{c} = (d_{\text{FR}}^{(k)}(p, r))_k$, we have $c_k \leq a_k + b_k$ component-wise, so $\|\mathbf{c}\|_2 \leq \|\mathbf{a} + \mathbf{b}\|_2 \leq \|\mathbf{a}\|_2 + \|\mathbf{b}\|_2$, the last step by the Minkowski inequality. Hence $d_{\text{FR}}(p, r) \leq d_{\text{FR}}(p, q) + d_{\text{FR}}(q, r)$.

(4) Invariance under sufficient statistics. By Čencov's theorem [51], the Fisher–Rao metric is (up to a constant multiple) the *unique* Riemannian metric on a statistical manifold that is invariant under all Markov morphisms, and in particular under sufficient statistics. A sufficient statistic T defines a Markov morphism (data processing), and Čencov's uniqueness result guarantees that the geodesic distance is preserved:

$$d_{\text{FR}}(p\theta, p\theta') = d_{\text{FR}}(p_T(\theta), p_T(\theta')).$$

For diagonal Gaussians, the sufficient statistics are $T(x) = (x_1, \dots, x_d, x_1^2, \dots, x_d^2)$, and the invariance ensures that the Fisher–Rao distance captures all statistically relevant information and nothing more.

(5) Computational complexity. Inspecting Equation (3), the computation requires:

- d log-ratio terms $\log(\sigma_{2,k}/\sigma_{1,k})$, each $O(1)$;
- d squarings of the log-ratio terms;
- d squared differences $(\mu_{1,k} - \mu_{2,k})^2$;
- d sum-of-squares denominators $\sigma_{1,k}^2 + \sigma_{2,k}^2$;
- d divisions for the mean terms;
- one running accumulator for the sum (no auxiliary array needed);
- one final square root.

This totals $2d$ additive terms, each requiring $O(1)$ arithmetic operations, plus one square root. The time complexity is $\Theta(d)$ and the auxiliary space is $\Theta(1)$ (a single accumulator variable). \square

A.2 Proof of Theorem 6.3 (Langevin Stationary Distribution)

Proof. We work on the Poincaré ball $(\mathbb{D}^d, g_{\mathbb{D}})$ with conformal factor $\lambda_{\xi} = 2/(1 - \|\xi\|^2)$ and metric tensor $g_{ij}(\xi) = \lambda_{\xi}^2 \delta_{ij}$.

Step 1: Fokker–Planck equation on a Riemannian manifold. The Riemannian Langevin SDE (Equation (17)) on (M, g) with potential U and temperature T generates a probability density $\rho(\xi, t)$ (with respect to the Riemannian volume form $dV_g = \sqrt{\det g} d\xi$) that evolves according to the Fokker–Planck equation (Equation (24)):

$$\frac{\partial \rho}{\partial t} = \nabla_g \cdot (\rho \nabla_g U) + T \Delta_g \rho,$$

where ∇_g is the Riemannian gradient, $\nabla_g \cdot$ is the Riemannian divergence, and $\Delta_g = \nabla_g \cdot \nabla_g$ is the Laplace–Beltrami operator.

For a conformal metric $g_{ij} = \lambda^2 \delta_{ij}$ on \mathbb{R}^d , the Riemannian gradient, divergence, and Laplacian have the explicit forms:

$$\nabla_g f = \lambda^{-2} \nabla_E f, \tag{32}$$

$$\nabla_g \cdot X = \frac{1}{\lambda^d} \nabla_E \cdot (\lambda^d X), \tag{33}$$

$$\Delta_g f = \lambda^{-2} \Delta_E f + (d-2) \lambda^{-3} \langle \nabla_E \lambda, \nabla_E f \rangle, \tag{34}$$

where ∇_E and Δ_E denote the Euclidean gradient and Laplacian, respectively. The Riemannian volume element is $\sqrt{\det g} = \lambda^d$.

Step 2: Gibbs ansatz. We claim the stationary density (with respect to dV_g) is

$$\rho_{\infty}(\xi) = \frac{1}{Z} \exp\left(-\frac{U(\xi)}{T}\right), \tag{35}$$

where $Z = \int_{\mathbb{D}^d} \exp(-U/T) dV_g$ is the partition function. Converting to the Lebesgue density on \mathbb{R}^d (i.e., the density with respect to $d\xi$), we obtain

$$\tilde{\rho}_{\infty}(\xi) = \rho_{\infty}(\xi) \sqrt{\det g} = \frac{\lambda_{\xi}^d}{Z} \exp\left(-\frac{U(\xi)}{T}\right) \propto \frac{1}{(1 - \|\xi\|^2)^d} \exp\left(-\frac{U(\xi)}{T}\right),$$

since $\lambda_\xi^d = (2/(1 - \|\xi\|^2))^d$ and the factor 2^d is absorbed into Z . This matches Equation (23).

Step 3: Verification that drift and diffusion cancel. We must show $\nabla_g \cdot (\rho_\infty \nabla_g U) + T \Delta_g \rho_\infty = 0$. Rewrite the Fokker–Planck equation in divergence form:

$$\frac{\partial \rho}{\partial t} = \nabla_g \cdot (\rho \nabla_g U + T \nabla_g \rho) = \nabla_g \cdot (\rho \nabla_g U + T \nabla_g \rho).$$

It suffices to show the flux $J = \rho_\infty \nabla_g U + T \nabla_g \rho_\infty$ vanishes identically. Compute $\nabla_g \rho_\infty$ using (35):

$$\nabla_g \rho_\infty = \nabla_g \left[\frac{1}{Z} \exp\left(-\frac{U}{T}\right) \right] = \frac{1}{Z} \exp\left(-\frac{U}{T}\right) \cdot \left(-\frac{1}{T}\right) \nabla_g U = -\frac{\rho_\infty}{T} \nabla_g U.$$

Substituting into the flux:

$$J = \rho_\infty \nabla_g U + T \left(-\frac{\rho_\infty}{T} \nabla_g U\right) = \rho_\infty \nabla_g U - \rho_\infty \nabla_g U = 0.$$

Since $J \equiv 0$, the divergence $\nabla_g \cdot J = 0$, confirming that ρ_∞ is a stationary solution.

Step 4: Integrability. We must verify $Z < \infty$ so that ρ_∞ is a proper probability density. By hypothesis, $U(\xi) \rightarrow \infty$ as $\|\xi\| \rightarrow 1$. Therefore, for any $\varepsilon > 0$, there exists $r_0 < 1$ such that $U(\xi) \geq M$ for all $\|\xi\| > r_0$, where M can be made arbitrarily large. Split the integral:

$$Z = \int_{\|\xi\| \leq r_0} \exp(-U/T) \lambda_\xi^d d\xi + \int_{r_0 < \|\xi\| < 1} \exp(-U/T) \lambda_\xi^d d\xi.$$

The first integral is over a compact set with a continuous integrand, hence finite. For the second, $\exp(-U/T) \leq \exp(-M/T)$ while $\lambda_\xi^d = (2/(1 - \|\xi\|^2))^d$ diverges as $\|\xi\| \rightarrow 1$. However, the Euclidean volume element of the annulus $\{r_0 < \|\xi\| < 1\}$ in polar coordinates contributes a factor $(1 - r^2)^0 \cdot r^{d-1} dr$. Since $U(\xi) \rightarrow \infty$ at the boundary, for any polynomial growth of λ_ξ^d , we can choose M large enough that $\exp(-M/T)$ suppresses the integrand. More precisely, $U(\xi) \rightarrow \infty$ as $\|\xi\| \rightarrow 1$ ensures that $\exp(-U(\xi)/T) \cdot \lambda_\xi^d \rightarrow 0$, making the integral convergent.

Step 5: Uniqueness. The Poincaré ball $(\mathbb{D}^d, g_{\mathbb{D}})$ is geodesically complete: every geodesic can be extended to infinite arc length (the boundary $\partial\mathbb{D}^d$ is at infinite geodesic distance from any interior point). On a geodesically complete Riemannian manifold, the Fokker–Planck operator with a confining potential ($U \rightarrow \infty$ at the boundary) generates a strongly continuous semigroup on $L^1(\mathbb{D}^d, dV_g)$, and the associated Markov process is non-explosive. By the theory of hypoelliptic diffusions on complete manifolds (see Hsu [22]), non-explosiveness combined with the existence of a Lyapunov function (here U itself, which satisfies $\Delta_g U$ is bounded above in compact sets and $U \rightarrow \infty$ at infinity) guarantees:

1. *Existence* of a stationary measure (proved in Step 2–3 above).
2. *Ergodicity*: the process visits every open set with positive probability (from the ellipticity of the generator, since the diffusion coefficient $\sqrt{2T} g^{-1/2}$ is everywhere non-degenerate on \mathbb{D}^d).
3. *Uniqueness*: an ergodic Markov process on a connected state space admits at most one stationary distribution.

Therefore ρ_∞ given by Equation (23) is the unique stationary distribution. \square

A.3 Proof of Theorem 6.5 (Optimal Progressive-Disclosure Depth)

Proof. We proceed in three steps: (i) derive the rate–distortion function for the source model, (ii) compute the number of levels under a constant distortion-reduction ratio, and (iii) establish the matching lower bound.

Step 1: Rate–distortion function. Let the memory source be $X \sim \mathcal{N}(0, \sigma^2 I_d)$ (the sub-Gaussian generalization follows at the end). Under squared-error distortion $d(x, \hat{x}) = \|x - \hat{x}\|^2 / d$ (per-coordinate average), the rate–distortion function (Equation (9)) for a scalar Gaussian source is

$$R(D) = \frac{1}{2} \log \frac{\sigma^2}{D}, \quad 0 < D \leq \sigma^2, \quad (36)$$

measured in nats (if $\log = \ln$) or bits (if $\log = \log_2$). At $D = \sigma^2$, $R = 0$ (no information needed to achieve source-variance distortion), and as $D \rightarrow 0$, $R \rightarrow \infty$ (perfect reconstruction requires infinite rate). For the d -dimensional i.i.d. Gaussian, the rate per symbol is still (36) by the additivity of rate–distortion for independent coordinates.

Step 2: Level-by-level rate accumulation. Progressive disclosure organizes the total representation into L levels, indexed $\ell = 0, 1, \dots, L$. Level $\ell = 0$ provides a “gist” at distortion $D_0 = D_{\max}$, and level $\ell = L$ provides the verbatim content at distortion $D_L = D_{\min}$. The distortion decreases geometrically:

$$D_\ell = D_{\max} \cdot r^{-\ell}, \quad r > 1,$$

so that each level reduces the distortion by the constant ratio r . The rate required to refine from level ℓ to $\ell + 1$ is

$$\begin{aligned} \Delta R_\ell &= R(D_{\ell+1}) - R(D_\ell) \\ &= \frac{1}{2} \log \frac{\sigma^2}{D_{\ell+1}} - \frac{1}{2} \log \frac{\sigma^2}{D_\ell} \\ &= \frac{1}{2} \log \frac{D_\ell}{D_{\ell+1}} \\ &= \frac{1}{2} \log r. \end{aligned}$$

Each refinement step adds exactly $\frac{1}{2} \log r$ nats, independent of the level ℓ .

The total number of levels satisfies $D_L = D_{\max} \cdot r^{-L} = D_{\min}$, giving

$$r^L = \frac{D_{\max}}{D_{\min}}, \quad L = \frac{\log(D_{\max}/D_{\min})}{\log r}.$$

With the normalization $D_{\max} = \sigma^2$ (the gist level uses no rate, matching $R(\sigma^2) = 0$), and $D_{\min} = \sigma^2/N$ (the fidelity increases with the number of stored memories):

$$L = \frac{\log(\sigma^2/(\sigma^2/N))}{\log r} = \frac{\log N}{\log r}.$$

Absorbing the constant $1/(2 \log r)$ from Equation (26) (where the factor of 2 accounts for using the full rate $R(D_{\min}) = \frac{1}{2} \log N$ divided into steps of $\frac{1}{2} \log r$ each), we obtain

$$D^*(N) = \frac{\log(D_{\max}/D_{\min})}{2 \log r} = \frac{\log N}{2 \log r} = \Theta(\log N).$$

Step 3: Lower bound (converse). By the converse of the rate–distortion theorem [13], any encoding that achieves expected distortion at most D_{\min} must use rate at least $R(D_{\min}) =$

$\frac{1}{2} \log(\sigma^2/D_{\min})$ nats per symbol. If this rate is distributed across L progressive levels with each level contributing at most $\frac{1}{2} \log r$ nats (the maximum per-level rate under the constant-ratio constraint), then

$$L \geq \frac{R(D_{\min})}{\frac{1}{2} \log r} = \frac{\log(\sigma^2/D_{\min})}{\log r}.$$

With $D_{\min} = \sigma^2/N$, this gives $L \geq \log N / \log r$, matching the upper bound. Hence $D^*(N) = \Theta(\log N)$.

Sub-Gaussian generalization. If X is sub-Gaussian with variance proxy σ^2 rather than exactly Gaussian, then $R_X(D) \leq R_{\mathcal{N}}(D) = \frac{1}{2} \log(\sigma^2/D)$ because the Gaussian maximizes the rate-distortion function over all sources with the same variance (Cover and Thomas [13], Theorem 10.3.3). The lower bound still holds (the converse applies to any source), so the depth bound $D^*(N) = \Theta(\log N)$ is unaffected. \square

A.4 Proof of Theorem 6.6 (Bounded Effective Memory Count)

Proof. We establish the bound $|\mathcal{M}_{\text{eff}}(t)| \leq C \cdot d^{d-1}$ in three steps: (i) characterize the fixed points of the Hopfield dynamics, (ii) relate the effective memory set to fixed-point basins, and (iii) apply the capacity result of Ramsauer et al. [41].

Step 1: Fixed points of the Hopfield update. The modern Hopfield energy (Equation (10)) for stored patterns $X = [\mu_1, \dots, \mu_M] \in \mathbb{R}^{d \times M}$ (with $\|\mu_i\| = 1$) and query state $\xi \in \mathbb{R}^d$ is

$$E(\xi, X) = -\frac{1}{\beta} \log \left(\sum_{i=1}^M e^{\beta \mu_i^\top \xi} \right) + \frac{1}{2} \|\xi\|^2 + \frac{1}{\beta} \log M + \frac{1}{2}.$$

The gradient is

$$\nabla_{\xi} E = \xi - X \text{softmax}(\beta X^\top \xi),$$

so a fixed point ξ^* of the update rule $\xi \mapsto X \text{softmax}(\beta X^\top \xi)$ satisfies $\nabla_{\xi} E(\xi^*) = 0$. At a fixed point near pattern μ_i , the softmax concentrates: $\text{softmax}(\beta X^\top \xi^*)_j \approx \delta_{ij}$ for large β , so $\xi^* \approx \mu_i$.

Step 2: Effective memories reside near fixed points. The effective memory set (Equation (27)) is $\mathcal{M}_{\text{eff}}(t) = \{m \in \mathcal{M}(t) : E(m, X(t)) \leq -\tau\}$. We show that each effective memory lies in the basin of attraction of some fixed point.

Since $\|\mu_i\| = 1$, the energy at a stored pattern μ_j is

$$\begin{aligned} E(\mu_j, X) &= -\frac{1}{\beta} \log \left(\sum_{i=1}^M e^{\beta \mu_i^\top \mu_j} \right) + \frac{1}{2} + \frac{1}{\beta} \log M + \frac{1}{2} \\ &= -\frac{1}{\beta} \log \left(e^{\beta} + \sum_{i \neq j} e^{\beta \mu_i^\top \mu_j} \right) + 1 + \frac{1}{\beta} \log M. \end{aligned}$$

For well-separated patterns with $\mu_i^\top \mu_j \leq 1 - \delta$ for $i \neq j$, the dominant term in the log-sum-exp is e^{β} , and the energy satisfies

$$E(\mu_j, X) \leq -1 + \frac{1}{\beta} \log M + \frac{M-1}{\beta} e^{-\beta\delta} + 1 = \frac{\log M}{\beta} + O(Me^{-\beta\delta}).$$

For β sufficiently large relative to $\log M$ (specifically $\beta > (2 \log M)/\delta$), the energy at each stored pattern is close to $-1 + \frac{\log M}{\beta}$, which is negative for $\beta > \log M$.

A memory m with $E(m, X) \leq -\tau$ must therefore have energy comparable to (or lower than) that of a stored pattern, placing m within the basin of attraction of some fixed point $\xi^* \approx \mu_i$ of the Hopfield dynamics. Different effective memories with energy below $-\tau$ must lie in different

basins (otherwise their energy would be higher due to interference), so $|\mathcal{M}_{\text{eff}}| \leq$ (number of fixed points).

Step 3: Storage capacity bound. The central result of Ramsauer et al. [41] (Theorem 3) states that the maximum number of patterns M^* in \mathbb{R}^d with $\|\mu_i\| = 1$ and pairwise inner products $\mu_i^\top \mu_j \leq 1 - \delta$ (for $i \neq j$) that can be stored as *well-separated* fixed points of the modern Hopfield update is bounded by

$$M^* \leq C_1(\delta, \beta) \cdot d^{d-1},$$

where C_1 depends on the separation parameter δ and the inverse temperature β . This follows from a covering number argument: the set of unit vectors in \mathbb{R}^d with pairwise angular separation at least $\arccos(1 - \delta)$ has cardinality bounded by the maximum δ -separated packing of the unit sphere S^{d-1} . The packing bound from Ramsauer et al. [41] gives $M^* = O(d^{d-1})$ (which, while exponential in d , reflects the exponential capacity advantage of modern over classical Hopfield networks).

Since each effective memory is associated with a unique fixed point (Step 2) and the number of fixed points is at most M^* (Step 3):

$$|\mathcal{M}_{\text{eff}}(t)| \leq M^* \leq C \cdot d^{d-1},$$

where $C = C_1(\delta, \beta)$ absorbs the dependence on δ (which is determined by the embedding model) and β (which is a system hyperparameter). Specifically,

$$C = \frac{1}{\text{Vol}(S^{d-1})} \cdot \left(\frac{\pi}{\arccos(1 - \delta)} \right)^{d-1} \cdot (1 + \varepsilon(\beta)),$$

where $\varepsilon(\beta) \rightarrow 0$ as $\beta \rightarrow \infty$ (in the low-temperature limit, the basins of attraction shrink to points and the capacity achieves the sphere-packing bound). \square

B Implementation Details

This appendix provides hyperparameter ranges, a retrieval pipeline overview, database schema summary, and compute requirements for reproducing the experiments in Section 7. Complete implementation details, exact configurations, and evaluation scripts are available in the open-source repository.

B.1 Hyperparameters

B.2 Retrieval Pipeline Overview

The retrieval pipeline proceeds in five stages, as described in Section 5.1: **(1) Query classification:** the query is classified into one of four types (single-hop, multi-hop, temporal, open-domain) and per-channel weight multipliers are assigned accordingly. **(2) Parallel channel search:** four independent channels (semantic, BM25, entity graph, temporal) execute in parallel, each producing a ranked candidate list. **(3) Fusion:** weighted reciprocal rank fusion (Eq. 11) merges the four lists into a single ranked set; profile lookup results and scene-expanded facts are added. **(4) Bridge discovery** (multi-hop queries only): cross-cluster connections are identified via graph traversal. **(5) Reranking:** a cross-encoder neural reranker produces the final blended score (Eq. 12) and the top- k candidates are returned. Complete implementation details are available in the open-source repository.

Table 6: System components and their configurable parameters. All values were determined via grid search on a held-out LoCoMo validation split. Exact configurations are available in the open-source repository; parameters may evolve across versions.

Component	Parameters	Notes
Channel weights	4 per-channel, query-type-dependent	Grid-search optimized
RRF fusion	Fusion constant k	Standard range per literature [12]
Cross-encoder blend	Query-type-dependent α	Higher for single-hop (Eq. 12)
BM25	k_1, b	Standard Okapi defaults
Fisher-information	Temperature, access threshold	Controls cosine→Fisher transition
Sheaf consistency	Contradiction threshold τ	Coboundary norm based
Entity graph	Walk depth, decay factor	Shallow walk, exponential decay
Mode A/B embedding	768-d local model	Pre-cached, zero network access
Mode C embedding	3072-d cloud model	API-based
Reranker	Cross-encoder model	Local neural reranker

B.3 Database Schema

All state is persisted in a single SQLite database (WAL mode). The schema comprises 21 tables organized into six groups: memory storage, knowledge graph, retrieval support, mathematical state, temporal tracking, and system configuration. All tables are partitioned by a profile identifier for multi-tenant isolation. The complete schema is available in the open-source repository.

B.4 Compute Requirements

We run experiments on Azure Container Instances (ACI), each allocated 2 vCPUs and 4 GB RAM. The Docker image (Python 3.12, PyTorch 2.10 CPU-only) includes pre-cached weights for the local embedding model and cross-encoder reranker, eliminating network dependency during Mode A execution. A total of 111 containers were deployed across three Azure subscriptions, each processing one (conversation, configuration) pair. The full evaluation covers 10 LoCoMo conversations with 8 ablation configurations. Six Azure OpenAI deployments serve the judge model and Mode C embeddings. Estimated total compute cost: \$9–15 USD. Retrieval scores in Mode A are fully deterministic; Mode C results are deterministic up to LLM non-determinism in judge scoring and answer generation.

C Additional Experimental Results

This appendix provides per-conversation breakdowns, Mode C detailed results, ablation completeness data, and a description of the re-scoring methodology used for Mode A Retrieval evaluation.

C.1 Per-Conversation Mode A Results

Table 7 reports the full Mode A Raw (`a_none`) scores for all ten LoCoMo conversations. Conversations marked *Partial* completed ingestion and retrieval but were interrupted during answer generation on a subset of questions; their scores reflect only the answered portion.

C.2 Mode C Detailed Results

Table 8 presents the per-category breakdown for Mode C on conv-30 (81 scored questions, fully completed). We additionally report the `cross_encoder_off` variant to quantify the cross-encoder

Table 7: Per-conversation Mode A Raw accuracy on LoCoMo. *Partial* indicates the container completed a subset of questions before timeout. Aggregate is the question-weighted mean across all 1,276 scored questions.

Conversation	Questions	Accuracy (%)	Status
conv-26	152	58.6	Done
conv-30	81	63.0	Done
conv-41	134	62.7	Partial
conv-42	149	55.7	Partial
conv-43	161	65.2	Partial
conv-44	123	64.2	Done
conv-47	130	56.9	Partial
conv-48	87	52.9	Partial
conv-49	156	62.2	Done
conv-50	103	61.2	Partial
Average	1,276	60.4	—

contribution in the cloud-augmented setting.

Table 8: Mode C per-category accuracy on conv-30 (81 questions). The `CE off` column disables cross-encoder reranking.

Category	Count	Mode C (%)	CE off (%)	Δ
Single-hop	11	64.0	55.0	-9.0
Multi-hop	26	100.0	100.0	0.0
Open-domain	44	86.0	93.0	+7.0
Aggregate	81	87.7	90.1	+2.4

The counter-intuitive improvement when removing the cross-encoder in Mode C (+2.4 pp) is driven by open-domain questions, where the cross-encoder occasionally demotes broadly relevant facts in favour of narrowly matching passages. Multi-hop accuracy remains perfect in both configurations, indicating that the cloud embedding quality (`text-embedding-3-large`, 3072-d) is the primary driver for relational reasoning at this conversation scale.

C.3 Re-Scoring Methodology

Mode A Retrieval scores (Tables 3 and 5) isolate retrieval quality from answer construction via a four-step protocol:

1. Run the full Mode A retrieval pipeline (four-channel fusion, cross-encoder reranking) to obtain the top- k context set.
2. Pass the retrieved context to `gpt-4.1-mini` with a focused answer-generation prompt identical to Mode C.
3. Re-judge the generated answer using the same LLM-as-Judge protocol (1–5 Likert scale, ≥ 4 threshold).
4. Record the binary score per question.

This re-scoring measures how much of Mode A Raw’s deficit is attributable to the absence of an LLM synthesiser versus an actual retrieval gap.

C.4 Entity Channel Ablation (Complete)

The `entity_off` ablation is the most complete ablation variant, covering all ten LoCoMo conversations (1,540 scored questions). [Table 9](#) reports the full results.

Table 9: `entity_off` ablation across all ten LoCoMo conversations. The entity graph channel is disabled; all other channels remain active. Average is question-weighted.

Conversation	Accuracy (%)	Questions
conv-26	50.0	152
conv-30	56.8	81
conv-41	66.4	152
conv-42	58.8	199
conv-43	58.4	178
conv-44	56.1	123
conv-47	64.7	150
conv-49	59.6	156
conv-50	61.4	158
Average	59.4	1,540

Comparing the entity-off average (59.4%) with the full-system average (60.4%, [Table 7](#)) yields a -1.0 pp delta consistent with the single-conversation ablation in [Table 4](#). The entity graph’s contribution is modest in aggregate but conversation-dependent: conv-26 shows the largest drop (-8.6 pp), likely because its dialogue structure involves densely interconnected entities where spreading activation provides the strongest complementary signal.